Available online at www.sciencedirect.com

SciVerse ScienceDirect

Procedia Engineering 00 (2012) 000–000

Procedia Engineering

www.elsevier.com/locate/procedia

5th BSME International Conference on Thermal Engineering

A review of flow and heat transfer in rotating microchannels

Pratanu Roy[a], N.K. Anand[a,*], Debjyoti Banerjee[a]

[a]*Department of Mechanical Engineering, Texas A&M University, College Station, TX 77840, USA*

Abstract

Rotating microchannels are integral part of centrifugally actuated miniaturized microfluidic devices, which have important applications in chemical analysis and biomedical diagnostics. As the field of centrifugal microfluidics continues to evolve, it is becoming imperative to understand the fundamental principles of fluid flow inside microchannels under the influence of centrifugal and Coriolis forces. These forces arise as a consequence of expressing the governing equations in rotating Eulerian reference frame and change the flow pattern significantly from the symmetric parabolic profile of a non-rotating channel. In this paper, we have summarized the recent advances in the area of fluid flow and heat transfer applications in radially rotating microchannels. A review of experimental and numerical studies available in the current literature is performed and issues with the applicability of analytical correlations for conventional macro-sized channels to describe the microscale flow phenomena have been discussed. From this state of the art review, it is evident that further systematic investigations are needed for a clear understanding of the transport mechanism associated with the flow and heat transfer inside rotating microchannels.

Keywords: Rotating microchannels; Centrifugal microfluidics; Secondary flow; Centrifugal force; Coriolis force.

Nomenclature

a	Width of the microchannel (m)	u_j	Velocity in j-direction (u, v, w for j = 1,2,3)
b	Height of the microchannel (m)	u,v,w	Velocities in x,y and z directions (m/s)
D_h	Hydraulic diameter of the microchannel (m)	x_i	Co-ordinates in i-direction (x, y, z for i = 1,2,3)
d_r	Radial distance of inlet from disk center (m)	*Greek Symbols*	
f_c	Coriolis force (N/ m^3)	α	Aspect ratio (= a/b)
f_ω	Centrifugal force (N/m^3)	β	Ratio of Coriolis force to centrifugal force
k	Thermal conductivity (W/m-K)	μ	Dynamic viscosity of fluid (Pa-s)
Kn	Knudsen number	ω	Rotation or angular velocity (rad/s)
L	Length of the microchannel (m)	*Subscripts*	
p	Pressure (Pa)	*avg*	Average
Re	Reynolds number	*cr*	Critical
Re_ω	Rotational Reynolds number	*i, j, k*	Array indices for tensor notation
RPM	Revolution per minute	*max*	Maximum
S_j	Source term in j-direction		
T	Temperature (^{o}C)		

* Corresponding author. Tel.: +1-979-845-5633; Fax: +1-979-845-4925.
E-mail address: nkanand@tamu.edu

1. Introduction

Investigation of fluid flow and heat transfer in rotating microchannels is important for centrifugally actuated microfluidic devices, which have enormous potential in the field of chemical analysis, drug delivery and biomedical applications. In these devices, an array of microchannels is etched on a compact-disk like circular substrate, which is then rotated at a certain frequency. By controlling the rotating frequency, various liquid handling processes, such as mixing, separation, routing, valving, siphoning, and droplet generation can be performed efficiently [1, 2]. This kind of arrangement is popularly known as *Lab-on-a-CD* or *LabCD* [1-3]. The objective of this compact disk like platform is to combine multiple liquid handling steps in order to perform all the bio-chemical processes in a flexible way [4].

A successful design of centrifugal microfluidic devices requires a clear understanding of fluid flow inside rotating microchannels. The physics of fluid flow through rotating microchannels is primarily governed by the pseudo forces, namely the centrifugal and the Coriolis forces, arising as a consequence of expressing the governing equations in rotating reference frame. At low rotation speed, the flow is purely driven by the centrifugal force. At higher rotation, the Coriolis force becomes dominant and a significant secondary flow can be observed perpendicular to the primary flow velocity. The effective operation of a centrifugal microfludic platform depends on regulating these forces in a controlled manner. For example, the working principle of capillary burst valve depends on the balance of centrifugal force and surface tension force [5]. On the other hand, mixing is enhanced in microchannels when the Coriolis force dominates over the centrifugal force [6]. The process becomes more complicated when heat transfer is included in the scenario. In some cases it is necessary to maintain the fluid within specific temperature ranges while rotating it inside the microchannel. For instance, the polymerase chain reaction (PCR) needs thermal homogeneity for efficient DNA hybridization [7]. In order to compute the correct temperature distribution of the fluid inside a rotating microchannel, the effect of rotation on convective heat transfer should be taken into consideration.

The flow physics in microscale can be modeled in two ways – one is by assuming it as a continuous medium with spatial and temporal variations of macroscopic flow quantities such as velocity, pressure, temperature or density and the other is by treating it as a collection of discrete particles whose flow properties are obtained by deterministic or probabilistic approaches [8]. The validity of Navier-Stokes equations to adequately describe the physics of flow inside microchannels depends upon the continuum hypothesis. Knudsen number (Kn), which is the ratio of the mean free path of the fluid molecules to the characteristic length, is often used as a validity indicator of the continuum hypothesis assumption [8-10]. For $Kn < 0.01$, the fluid can be considered as a continuum. As the Knudsen number approaches unity the continuum equations begin to fail, but for $Kn < 0.1$ the no slip boundary condition can still be adjusted using a slip parameter. The region ($0.01 < Kn < 0.1$) is called the "slip regime", to distinguish it from the transition regime ($0.1 < Kn < 10$), in which the Boltzmann equations are solved directly to predict flows.

For biological liquids, such as blood, plasma, urine, and for water, Knudsen number (Kn) falls well within the continuum region, where Navier-Stokes equations with no slip boundary conditions are applicable for any practical range of microchannel size. However, even for water flow in microchannels, contradictory results on the validity of the Navier-Stokes equations have been reported in the literature. Garimella and Sobhan [11] conducted a comparative study on the transport in microchannels and concluded that analyses based on Navier-Stokes and energy equations can adequately predict the flow and heat transfer characteristics in microchannel having a hydraulic diameter greater than 50 μm, provided that the experimental conditions and measurements are correctly identified and simulated. Another critical review on single phase liquid friction factors in microchannels was performed by Steinke and Kandlikar [12]. By analyzing over 150 papers that directly deal with the pressure drop measurements in the microchannels, they generated a database of over 5000 data points with the Reynolds number ranging from 0.002 to 5000 and hydraulic diameter ranging from 8 μm to 990 μm. They argued that, the studies which reported a deviation of friction factor from conventional theory did not account for the developing region or exit effect in the microchannel. Therefore, it was concluded that, the classical correlations are reliable in predicting the flow and heat transfer phenomena in microchannel as long as the entrance or exit effect and the experimental uncertainties are taken into account.

If the continuum hypothesis is also valid for centrifugally driven micro-flows, then the analysis of flow and heat transfer will not differ from that in rotating macro sized channels. In this article, we will focus on how the fluid flow and heat transfer characteristics inside rotating microchannels are used in the area of centrifugal microfluidics. Section 2 presents the recent reviews and trend of centrifugal microfluidics. Section 3 describes the working principle of a typical centrifugal microfluidic platform. Various applications of rotating microchannels in centrifugal microfluidics have been discussed in section 4. The final section summarizes the review and briefs about the future recommendations on this topic.

2. Recent literature review

Figure 1 shows the number of papers containing the term *centrifugal microfluidics* in the recent years. The results were compiled using the database of Web of Science, Elsevier, MEDLINE, IOP Electronic Journals, Health Reference Center

Academic, Directory of Open Access Journals, BioMed Central and American Chemical Society. Over the past decade, a steady increase of interest on the topic of centrifugal microfluidics can clearly be observed.

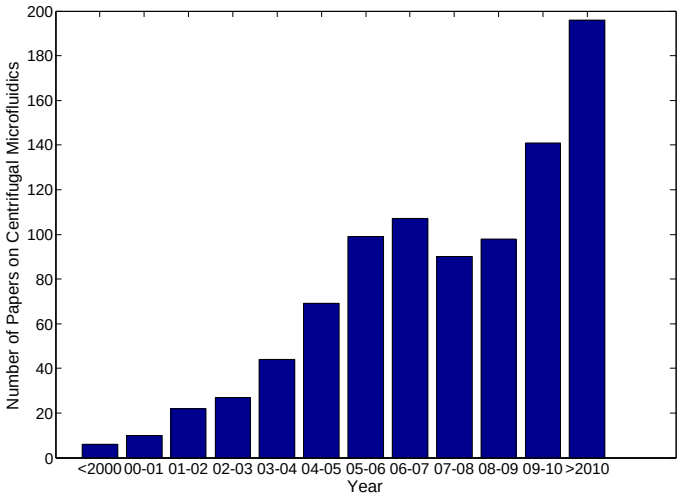

Fig. 1. Growth of publications on centrifugal microfluidics in the recent years

Comprehensive reviews on centrifugal microfluidics for biomedical applications can be found in [1, 13]. These reviews highlighted the recent progress in the relevant field and outlined the potential for future applications. Another review on centrifugal microfluidic and bio-optical disks can be found in [14]. The present review will emphasize on the more recent advances on centrifugal microfluidics. Selected literatures on the applications of centrifugal microfluidics are given in Appendix A.

3. Working principle

In most of the centrifugal microfluidic devices, the fluid is placed in a microchamber, which is connected to another reservoir through a microchannel. Figure 2 shows a schematic diagram of an array of rectangular microchannels aligned radially on a circular disk and a single microchannel on a rotating disk with corresponding forces acting on the flow. As the disk is rotated around an axis perpendicular to the plane of the disk, a centrifugal force f_ω is induced in the radially outward direction and the liquid advances through the microchannels towards the outlet. At this stage, the velocity of the liquid and the shape of the liquid meniscus are primarily governed by the centrifugal force and the surface tension force. Once the microchannel is filled up with the liquid, a continuous stream of liquid flow is established along the microchannel and the surface tension effect can be neglected. Due to the rotation, a Coriolis force f_c is also induced perpendicular to the centrifugal force on the disk plane. This Coriolis force is responsible for generating secondary flow phenomena in rotating microchannel flow.

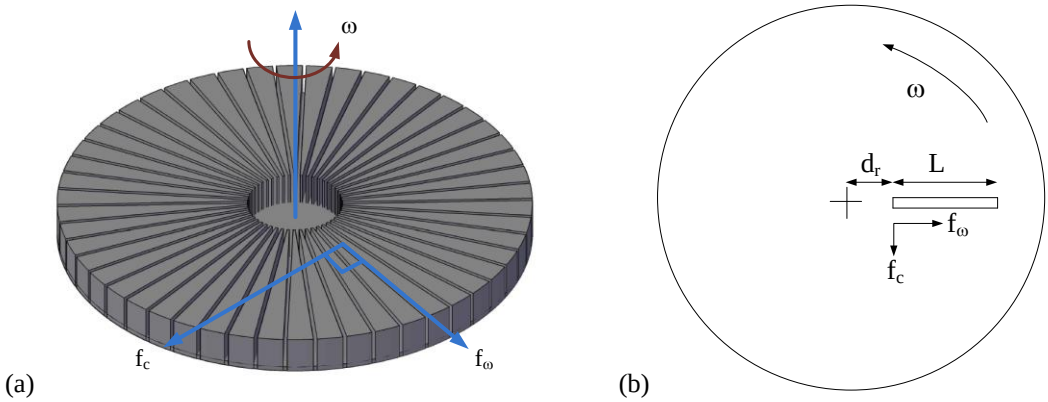

Fig. 2. Schematic of working principle : (a) an array of microchannels (b) simplified rotating disk with a single microchannel

If an unsteady, laminar, incompressible flow with constant thermo-physical properties and negligible buoyancy force is assumed, then the governing equations for microchannel flow with a generic forcing term S_j, can be written in the following Cartesian tensor form:

Continuity: $$\frac{\partial u_i}{\partial x_i} = 0 \quad (1)$$

Momentum: $$\rho\left(\frac{\partial u_j}{\partial t} + u_i\frac{\partial u_j}{\partial x_i}\right) = -\frac{\partial p}{\partial x_j} + \mu\left(\frac{\partial^2 u_j}{\partial x_i \partial x_i}\right) + \rho S_j \quad (2)$$

Energy: $$\rho C_p\left(\frac{\partial T}{\partial t} + u_i\frac{\partial T}{\partial x_i}\right) = \frac{\partial}{\partial x_i}\left(-k\frac{\partial T}{\partial x_i}\right) \quad (3)$$

For i, j = 1, 2, 3, $x_1 \in (0,a), x_2 \in (0,b), x_3 \in (0,L)$. Here, a, b and L are the width, height and length of the channel respectively. If we consider Cartesian velocity components u, v, w in x, y, z directions in place of u_1, u_2, u_3 velocities in x_1, x_2, x_3 directions, then the source terms in the momentum equations for an orthogonal rotation mode becomes [15]:

x-direction: $$S_1 = -2\omega w + \omega^2 x \quad (4)$$

y-direction: $$S_2 = 0 \quad (5)$$

z-direction: $$S_3 = 2\omega u + \omega^2(d_r + z) \quad (6)$$

Two non-dimensional numbers, namely flow Reynolds number (*Re*) and rotational Reynolds number (Re_ω) characterize the physics of rotating channel flows. Reynolds number ($Re = \rho w_{avg} D_h/\mu$) is the ratio of the inertial force to viscous force and rotational Reynolds number ($Re_\omega = \rho\omega D_h^2/\mu$) is the ratio of the rotating force to the viscous force. If a parabolic axial velocity profile is assumed in the primary flow direction, then it can be shown that the axial velocity (w) is in the order of ($\sim\rho\omega^2 D_h^2 d_r/8\mu$) [16]. Thus, the ratio of the Coriolis force $(2\rho\omega w)$ and the centrifugal force $(\rho\omega^2 d_r)$ becomes $\beta=\rho\omega D_h^2/8\mu$, which is a multiple of rotational Reynolds number Re_ω. This indicates that, a high rotational Reynolds number will induce high Coriolis force resulting in a strong secondary flow.

4. Review of rotating microchannel applications

In this section we present a review of the recent applications of rotating microchannel in centrifugal microfluidics area.

4.1. Centrifugal pumping

Centrifugal pumping occurs when the liquid flows from the reservoir into the microchannels due to the centrifugal force (as described in section 3). Duffy et al. [17] measured the experimental flow rate during centrifugal pumping inside microchannels of different widths (20 – 500 μm), depths (16 – 340 μm), and lengths (12.5-182 mm) subjected to a range of rotational frequencies (400-1600 RPM). They compared the experimental flow rate with the Hagen-Poiseuille flow rate in a log-log graph and showed that centrifugally driven microchannel flows can be treated as Hagen-Poiseuille flows for a wide range of attributes. Madou et al. [18] measured the pressure drop against the flow rate relationship for two different microchannels (one 150 μm wide and 34 μm deep, and the other 50 μm wide and 34 μm deep). They also showed that the flow rate *Q* can be predicted with Hagen-Poiseuille equation: $Q = \pi D_h^4 \Delta P/128\mu L$. For a purely centrifugal flow, the pressure difference ΔP between the channel inlet and outlet can be expressed by: $\Delta P = \rho\omega^2 r_{av}\Delta r$. Sine, $Q = w_{avg}A$, the average velocity $w_{avg} = \rho\omega^2 r_{av}\Delta r D_h^2/32\mu L$. Here, r_{av} is the average distance of the liquid from the disk center and Δr is the radial extent of the fluid. For rectangular microchannels, a better approximation for velocity can be derived by neglecting the non-linear convective terms and Coriolis force terms in the Navier-Stokes equations and then solving the resulting Poisson equation with a modified pressure-gradient [19]. All these approximations may work well for low rotational Reynolds number ($Re_\omega \sim O(1)$). However, for high rotational Reynolds number, the Coriolis force can change the velocity profile significantly from these relations and then the effect of secondary flow should be taken into account.

In order to illustrate how the flow in centrifugal pumping are affected by the rotation, the steady state governing equations were solved numerically for radially rotating rectangular microchannels of different aspect ratios ($\alpha = a/b$) with hydraulic diameter D_h = 200μm and Re = 100. The details of the numerical solver used for the simulation can be found in [20]. Figure 3 presents the deviation of the friction relation of a rotating channel flow from that of a non-rotating channel flow. The friction factor (*f*) or the friction relation (*fRe*) can be considered a measure of the pumping power required to drive the centrifugal flow. From Figure 3, it can be observed that, as the rotational speed (RPM) or the rotational Reynolds number (Re_ω) increases, the percentage deviation of the friction relation of a rotating channel flow from that of a non-

rotating channel flow increases. Moreover, for a fixed rotational Reynolds number, this deviation is low for wide aspect ratio channels, whereas the deviation is high for low aspect ratio channels. It indicates that, for rectangular channels, channel height might be a better representative of the characteristic length than the hydraulic diameter.

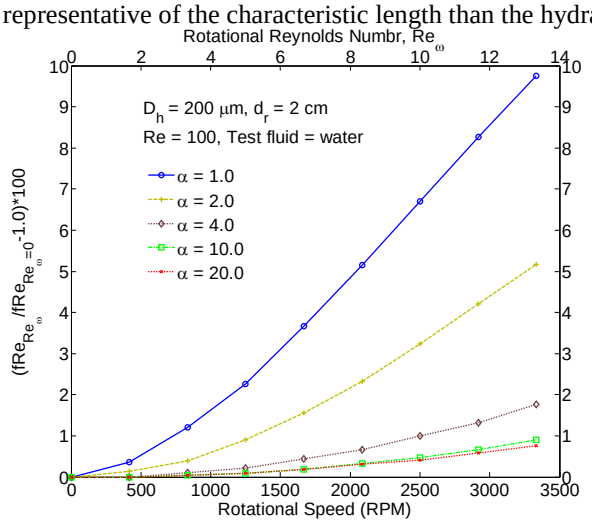

Fig. 3. Deviation of friction relation *(fRe)* of rotating microchannels from that of non-rotating microchannels

In practice, for microfluidic devices, it is not possible to simultaneously control both the rotational speed and Reynolds number. In most of the centrifugal microfluidics devices, the fluid is kept in a reservoir and the disk is rotated at a certain rotating frequency. As a result, fluid from reservoir flows through the microchannel due to the centrifugal force just like a pressure driven flow occurs due to the pressure difference at channel inlet and outlet. Once the rotating frequency is fixed, the velocity (and the Reynolds number) of the fluid inside the microchannel is also fixed. Thus, the rotating speed and the Reynolds number or fluid velocity is coupled in a centrifugally driven flow. In order to account for this coupled nature, the average velocity of the fluid was calculated using the analytical solution of a purely centrifugal flow in rectangular channel with zero pressure-gradient [21]. Figure 4 presents the comparison of velocity profiles of steady rotating channel flows with the analytical results for different rotational Reynolds number. By inspecting this figure, it can be observed that, for low rotational Reynolds number (Re_ω = 1.67, RPM = 400), the velocity profiles are very close to the analytical results. However, for large rotational Reynolds number (Re_ω = 17.86, RPM = 4200), the velocity profiles deviate significantly from the symmetric parabolic flow profiles proposed by the analytical solutions. Thus, although the existing analytical solutions of centrifugal flow can be used to predict the flow parameters, care should be taken to consider the uncertainty introduced by these approximations at large rotational Reynolds number.

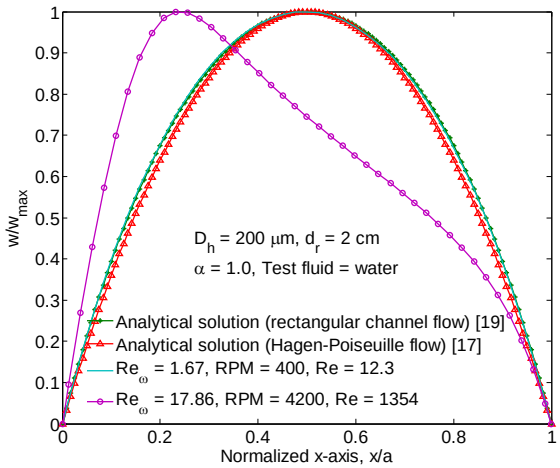

Fig. 4. Comparison of outlet velocity profiles of rotating microchannels with approximate analytical solutions

4.2. Mixing

Due to the small length scale of microfluidic devices, the Reynolds number is typically in the laminar flow regime. As a result, mixing in microscale is primarily dominated by diffusion process, which is time-consuming. In centrifugal microfluidic platform, rapid mixing can be achieved by alternate rotation (clockwise and counter-clockwise) of the microchambers containing the mixture [22, 23]. The mixing process can be further enhanced by pre-filling the mixing chambers with paramagnetic beads and placing a permanent magnet underneath it to induce a magnetic stirring [22, 24, 25]. An alternative approach to these methods is to induce strong secondary flow resulting from Corolis force at high rotational speeds [6, 16]. In a recent study on the characteristics of two fluid mixing in rotationally actuated T-shaped microchannel, Chakraborty et al. [26] identified three distinct mixing regimes based on the change of mixing patterns with the change of β. The three regimes are – (i) diffusion based mixing (at low rotation speeds, $0 < \beta < 1.0$), (ii) Coriolis force based mixing (at intermediate rotation speeds, $1.0 < \beta < 2.0$), and (iii) mixing based on flow instability (at high rotation speeds, $\beta > 2.0$). It is interesting to note that, although Coriolis force based mixing regime starts at $\beta = 1.0$, the efficient mixing occurs when β exceeds 1.35 that is when $Re_\omega > 10.8$. From the definition of rotational Reynolds number Re_ω,it can be seen that, Re_ωvaries with the square of the hydraulic diameter D_h. Thus, to attain an effective Coriolis based mixing, one should choose relatively large scale channel dimensions so that Re_ω is sufficiently high to impact the transverse flow.

By solving the governing equations numerically, we can determine for what values of rotational Reynolds number the effect of rotation is significant. Figure 5 shows the variation of friction relations for rotating microchannels in comparison to non-rotating microchannels for a range of Reynolds number and rotational Reynolds number. The case with aspect ratio α = 9.09 corresponds to the geometry used in the experiment of Chakraborty et al. [26]. From this graph, it can be seen that, as the rotational Reynolds number increases, the secondary flow effect increases and the friction factor deviates from the value of its non-rotating counterpart. From the numerical data, it was found that, one percent deviation in friction relation produces a secondary flow in an amount of 2-3% of the average velocity. In case of low rotational speed, the centrifugal flow has low Reynolds number and consequently the secondary flow will be negligible. But, high rotational speed will result in a high Reynolds number flow which will in turn induce a large secondary flow. If 1% deviation in *fRe* is considered as a critical value above which the effect of Coriolis force will be significant, then a demarcation line can been drawn in Figure 5 to differentiate between the diffusion dominated region and secondary flow dominated region. A corresponding critical value for rotational Reynolds number ($Re_{\omega,cr}$) can be derived from the diagram. For α = 9.09, $Re_{\omega,cr} = 10.2$, which is very close to the value reported by Chakraborty et al. ($\beta = 1.35$, $Re_\omega = 10.8$) [26]. For other aspect ratios, critical rotational Reynolds number can be derived in a similar way.

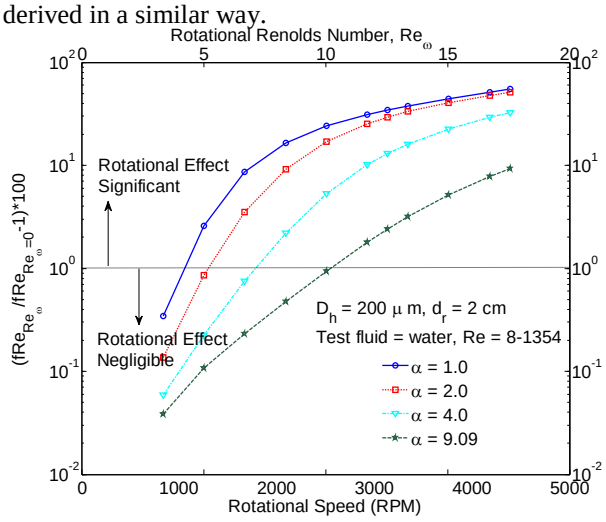

Fig. 5. Identification of significant secondary flow dominant regions and critical rotational Reynolds number

Other methods of mixing in rotating microchannels have also been reported. Micromixing of liquids by pneumatic agitation on centrifugal microfluidic platform was recently reported by Kong et al. [27]. A stream of compressed gas was applied to agitate the liquids and a 30-fold improvement in mixing was observed over a range of rotational frequencies (450-1500 RPM) compared to the conventional diffusion-based mixing.

4.3. Valving

By exploiting the capillary effect and the wetting nature of the channel surface, passive microfluidic valve can be constructed without any moving parts. Capillary valves are operated using the developed pressure barrier when the capillary flow channel undergoes a sudden expansion in cross-section [5]. Figure 6a demonstrates a capillary valve, where the bursting frequency depends on the balance between surface tension induced pressure and centrifugally induced pressure [13]. The critical burst condition refers to the condition when the centrifugally induced pressure reaches the surface tension induced pressure and the capillary valve opens. By balancing these two pressures a simple analytical relation among critical (bursting) frequency (ω_{cr}), surface tension (σ) and characteristic length (D_h) can be deduced: $\rho\omega_{cr}^2 r_{av}\Delta r > 4\sigma/D_h$ [5, 28-30].

Depending on the wetting nature of the surface, the microchannel surface can be either hydrophilic or hydrophobic. A hydrophilic surface has a strong affinity to water with a contact angle less than 90^o. On the other hand, due to large contact angles ($>90^o$) and the repelling nature of a hydrophobic surface, water do not stick to it. Capillary bust valves are made of hydrophilic microchannels. Another type of valving used in centrifugal microfluidics is hydrophobic valving, where a small hydrophobic channel is placed right after the microchamber to restrict the fluid movement (refer to Figure 6b) [2].

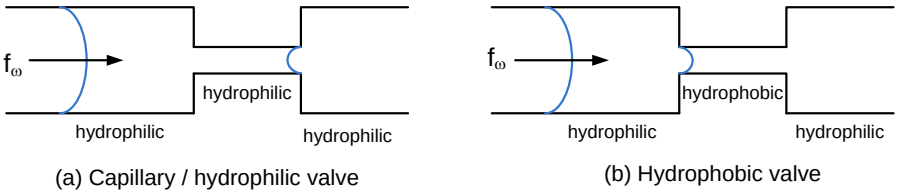

(a) Capillary / hydrophilic valve (b) Hydrophobic valve

Fig. 6. Schematic of: (a) Capillary valve (b) Hydrophobic valve (Redrawn from [2])

4.4. Directional Switching

In a rotating microchannel, the effect of Coriolis force is to generate a transverse velocity component perpendicular to the main flow direction, the sign of which depends on the sense of rotation. The transverse or secondary flow can be used to generate directional switching at high spinning frequencies [31-33]. Figure 7 shows an example of directional switching in Y-shaped structure, which is also known as 'passive flow switching valve' [32].

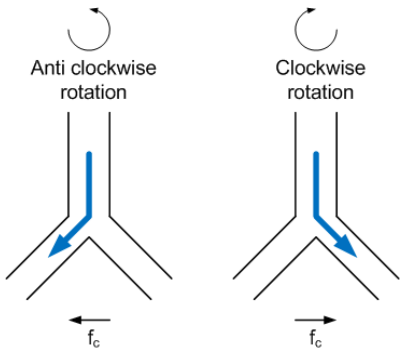

Fig. 7. Directional switching based on Coriolis force and sense of rotation (adapted from [23])

Another form of flow switching on centrifugal microfluidic platform can be achieved by using a regulated stream of compressed gas. Kong et al. [34] implemented this technique to control the flow at a T-junction for relatively low rotational frequencies (400-1200 RPM).

4.5. PCR Amplification

During Nucleic acid (NA) analysis, a common step is to amplify Polymerase Chain Reaction, or PCR. This requires repeated thermocycling of the analyte NA in a microchamber [7] i.e. the reaction volume is maintained under prescribed temperature zones, typically 90^o-94^oC for denaturation (that causes DNA melting by disrupting the hydrogen bonds), 50^o-70^oC for renaturation (i.e. annealing) and 70^o-90^oC for extension. By using the secondary flow effect, thermal homogeneity can be achieved in PCR amplification on a spinning disk. Aamsia et al. [35] demonstrated an automated centrifugal

microfluidic system for PCR amplification using novel thermoelectric heating and ice-valves. Seigrist et al. [7] numerically and experimentally analyzed the rotating PCR microchamber filling behavior at different inlet pressure boundary conditions (0.5 kPa to 2.0 kPa). They showed that, due to the induced centrifugal and Coriolis force, the nature of chamber filling is different for rotating case from that of non-rotating case.

5. Summary

In this paper, we have summarized the recent advances in the applications of radially rotating microchannels. A review of experimental and numerical studies available in the current literature was performed. The applicability of analytical correlations for conventional macro-sized channels to describe the rotating microchannel flow phenomena has been discussed. Numerical results showed that, for low rotational Reynolds number, the effect of Coriolis force is small and the existing analytical solutions for fully developed pipe or channel flow can be used. However, for high rotational Reynolds number, the deviation of flow parameters in rotating microchannel flow can be significant and the uncertainty introduced by using the analytical results can be high. By comparing the friction relation of a centrifugally driven flow from that of a non-rotating channel flow, a critical rotational Reynolds number ($Re_{\omega,cr}$) can be identified, above which the effect of rotation is significant. However, a clear picture of flow regimes showing where the secondary flow effect is considerably high is still missing. Thus, it is evident that further systematic investigations are needed to find out the range Reynolds number (Re) and rotational Reynolds number (Re_{ω}), for which the secondary flow inside rotating microchannels can be considered significant.

References

[1] Madou, M., Zoval, J., Jia, G., Kido, H., Kim, J., and Kim, N., 2006, "Lab on a Cd," Annu. Rev. Biomed. Eng., 8(pp. 601-628.
[2] Ducrée, J., Haeberle, S., Lutz, S., Pausch, S., Von Stetten, F., and Zengerle, R., 2007, "The Centrifugal Microfluidic Bio-Disk Platform," Journal of Micromechanics and Microengineering, 17(7), pp. S103.
[3] Madou, M. J., and Kellogg, G. J., 1998, "The Labcd: A Centrifuge-Based Microfluidic Platform for Diagnostics," Proc. Systems and Technologies for Clinical Diagnostics and Drug Discovery, Vol. 3259, pp. 80-93.
[4] Mark, D., Haeberle, S., Roth, G., Von Stetten, F., and Zengerle, R., 2010, "Microfluidic Lab-on-a-Chip Platforms: Requirements, Characteristics and Applications," Chem. Soc. Rev., 39(3), pp. 1153-1182.
[5] Zeng, J., Banerjee, D., Deshpande, M., Gilbert, J. R., Duffy, D. C., and Kellogg, G. J., 2000, "Design Analyses of Capillary Burst Valves in Centrifugal Microfluidics," μTAS 2000 Symposium, Enschede, Netherlands, May 14-18, 2000.
[6] Ducrée, J., Haeberle, S., Brenner, T., Glatzel, T., and Zengerle, R., 2006b, "Patterning of Flow and Mixing in Rotating Radial Microchannels," Microfluidics and Nanofluidics, 2(2), pp. 97-105.
[7] Siegrist, J., Amasia, M., Singh, N., Banerjee, D., and Madou, M., 2010, "Numerical Modeling and Experimental Validation of Uniform Microchamber Filling in Centrifugal Microfluidics," Lab Chip, 10(7), pp. 876-886.
[8] Gad-El-Hak, M., 1999, "The Fluid Mechanics of Microdevices-the Freeman Scholar Lecture," Transactions - ASME Journal of Fluids Engineering, 121(pp. 5-33.
[9] Gad-El-Hak, M., 2002, *The Mems Handbook*, CRC Pr I Llc,
[10] Bontemps, A., 2005, "Measurements of Single-Phase Pressure Drop and Heat Transfer Coefficient in Micro and Minichannels," Microscale Heat Transfer Fundamentals and Applications, pp. 25-48.
[11] Garimella, S. V., and Sobhan, C., 2003, "Transport in Microchannels–a Critical Review," Ann. Rev. Heat Transfer, 13(pp. 1–50.
[12] Steinke, M. E., and Kandlikar, S. G., 2006, "Single-Phase Liquid Friction Factors in Microchannels," International journal of thermal sciences, 45(11), pp. 1073-1083.
[13] Gorkin, R., Park, J., Siegrist, J., Amasia, M., Lee, B. S., Park, J. M., Kim, J., Kim, H., Madou, M., and Cho, Y. K., 2010, "Centrifugal Microfluidics for Biomedical Applications," Lab Chip, 10(14), pp. 1758-1773.
[14] Nolte, D. D., 2009, "Invited Review Article: Review of Centrifugal Microfluidic and Bio-Optical Disks," Review of Scientific Instruments, 80(10), pp. 101101-101101-22.
[15] Morris, W. D., 1981, *Heat Transfer and Fluid Flow in Rotating Coolant Channels*, Research Studies Press,
[16] Ducree, J., Brenner, T., Haeberle, S., Glatzel, T., and Zengerle, R., 2006, "Multilamination of Flows in Planar Networks of Rotating Microchannels," Microfluidics and Nanofluidics, 2(1), pp. 78-84.
[17] Duffy, D. C., Gillis, H. L., Lin, J., Sheppard Jr, N. F., and Kellogg, G. J., 1999, "Microfabricated Centrifugal Microfluidic Systems: Characterization and Multiple Enzymatic Assays," Analytical Chemistry, 71(20), pp. 4669-4678.
[18] Madou, M. J., Lee, L. J., Daunert, S., Lai, S., and Shih, C. H., 2001, "Design and Fabrication of Cd-Like Microfluidic Platforms for Diagnostics: Microfluidic Functions," Biomedical Microdevices, 3(3), pp. 245-254.

[19] Chakraborty, D., Gorkin, R., Madou, M., Kulinsky, L., and Chakraborty, S., 2009, "Capillary Filling in Centrifugally Actuated Microfluidic Devices with Dynamically Evolving Contact Line Motion," Journal of Applied Physics, 105(8), pp. 084904-084904-10.
[20] Roy, P., Anand, N. K., and Banerjee, D., 2011, "A Numerical Study of Unsteady Laminar Flow and Heat Transfer through an Array of Rotating Rectangular Microchannels," ASME Conference Proceedings, 2011(54921), pp. 1141-1145.
[21] Liu, M., Zhang, J., Liu, Y., Lau, W., and Yang, J., 2008, "Modeling of Flow Burst, Flow Timing in Lab-on-a-Cd Systems and Its Application in Digital Chemical Analysis," Chemical Engineering & Technology, 31(9), pp. 1328-1335.
[22] Grumann, M., Geipel, A., Riegger, L., Zengerle, R., and Ducree, J., 2005, "Batch-Mode Mixing on Centrifugal Microfluidic Platforms," Lab on a Chip, 5(5), pp. 560-565.
[23] Noroozi, Z., Kido, H., Micic, M., Pan, H., Bartolome, C., Princevac, M., Zoval, J., and Madou, M., 2009, "Reciprocating Flow-Based Centrifugal Microfluidics Mixer," Review of Scientific Instruments, 80(7), pp. 075102-075102-8.
[24] Steigert, J., Grumann, M., Brenner, T., Mittenbühler, K., Nann, T., Rühe, J., Moser, I., Haeberle, S., Riegger, L., and Riegler, J., 2005, "Integrated Sample Preparation, Reaction, and Detection on a High-Frequency Centrifugal Microfluidic Platform," Journal of the Association for Laboratory Automation, 10(5), pp. 331-341.
[25] Kido, H., Micic, M., Smith, D., Zoval, J., Norton, J., and Madou, M., 2007, "A Novel, Compact Disk-Like Centrifugal Microfluidics System for Cell Lysis and Sample Homogenization," Colloids and Surfaces B: Biointerfaces, 58(1), pp. 44-51.
[26] Chakraborty, D., Madou, M., and Chakraborty, S., 2011, "Anomalous Mixing Behaviour in Rotationally Actuated Microfluidic Devices," Lab Chip, 11(17), pp. 2823-2826.
[27] Kong, M. C. R., and Salin, E. D., 2012, "Micromixing by Pneumatic Agitation on Continually Rotating Centrifugal Microfluidic Platforms," Microfluidics and Nanofluidics, pp. 1-7.
[28] Cho, H., Kim, H. Y., Kang, J. Y., and Kim, T. S., 2007, "How the Capillary Burst Microvalve Works," Journal of Colloid and Interface science, 306(2), pp. 379-385.
[29] Badr, I. H. A., Johnson, R. D., Madou, M. J., and Bachas, L. G., 2002, "Fluorescent Ion-Selective Optode Membranes Incorporated onto a Centrifugal Microfluidics Platform," Analytical Chemistry, 74(21), pp. 5569-5575.
[30] Chen, J. M., Huang, P. C., and Lin, M. G., 2008, "Analysis and Experiment of Capillary Valves for Microfluidics on a Rotating Disk," Microfluidics and Nanofluidics, 4(5), pp. 427-437.
[31] Brenner, T., Glatzel, T., Zengerle, R., and Ducree, J., 2003, "A Flow-Switch Based on Coriolis Force," Proceedings of the 7th international conference on micro total analysis systems (μTAS 2003), 2003, pp. 5-9.
[32] Kim, J., Kido, H., Rangel, R. H., and Madou, M. J., 2008, "Passive Flow Switching Valves on a Centrifugal Microfluidic Platform," Sensors and Actuators B: Chemical, 128(2), pp. 613-621.
[33] Brenner, T., Glatzel, T., Zengerle, R., and Ducrée, J., 2004, "Frequency-Dependent Transversal Flow Control in Centrifugal Microfluidics," Lab Chip, 5(2), pp. 146-150.
[34] Kong, M. C. R., and Salin, E. D., 2011, "Pneumatic Flow Switching on Centrifugal Microfluidic Platforms in Motion," Analytical Chemistry, 83(3), pp. 1148-1151.
[35] Amasia, M., Cozzens, M., and Madou, M. J., 2011, "Centrifugal Microfluidic Platform for Rapid Pcr Amplification Using Integrated Thermoelectric Heating and Ice-Valving," Sensors and Actuators B: Chemical, pp.
[36] Ukita, Y., Kondo, S., Azeta, T., Ishizawa, M., Kataoka, C., Takeo, M., and Utsumi, Y., 2012, "Stacked Centrifugal Microfluidic Device with Three-Dimensional Microchannel Networks and Multifunctional Capillary Bundle Structures for Immunoassay," Sensors and Actuators B: Chemical, pp.
[37] Gorkin, R., Soroori, S., Southard, W., Clime, L., Veres, T., Kido, H., Kulinsky, L., and Madou, M., 2012, "Suction-Enhanced Siphon Valves for Centrifugal Microfluidic Platforms," Microfluidics and Nanofluidics, pp. 1-10.
[38] Burger, R., Kirby, D., Glynn, M., Nwankire, C., O'sullivan, M., Siegrist, J., Kinahan, D., Aguirre, G., Kijanka, G., and Gorkin, R. A., 2012, "Centrifugal Microfluidics for Cell Analysis," Current Opinion in Chemical Biology, pp.
[39] Burger, J., Gross, A., Mark, D., Von Stetten, F., Zengerle, R., and Roth, G., 2011, "IR Thermocycler for Centrifugal Microfluidic Platform with Direct on-Disk Wireless Temperature Measurement System," *16th International Conf. on Solid-State Sensors, Actuators and Microsystems Conference (TRANSDUCERS), 2011*, vol., no., pp.2867-2870, 5-9 June 2011.
[40] Moore, J. L., Mccuiston, A., Mittendorf, I., Ottway, R., and Johnson, R. D., 2011, "Behavior of Capillary Valves in Centrifugal Microfluidic Devices Prepared by Three-Dimensional Printing," Microfluidics and Nanofluidics, 10(4), pp. 877-888.
[41] Kong, M. C. R., and Salin, E. D., 2011, "A Valveless Pneumatic Fluid Transfer Technique Applied to Standard Additions on a Centrifugal Microfluidic Platform," Analytical Chemistry, 83(23), pp. 9186-9190.
[42] Abi-Samra, K., Clime, L., Kong, L., Gorkin, R., Kim, T. H., Cho, Y. K., and Madou, M., 2011, "Thermo-Pneumatic Pumping in Centrifugal Microfluidic Platforms," Microfluidics and Nanofluidics, 11(5), pp. 643-652.
[43] Mark, D., Weber, P., Lutz, S., Focke, M., Zengerle, R., and Von Stetten, F., 2011, "Aliquoting on the Centrifugal Microfluidic Platform Based on Centrifugo-Pneumatic Valves," Microfluidics and Nanofluidics, 10(6), pp. 1279-1288.
[44] Wang, L., Kropinski, M. C., and Li, P. C. H., 2011, "Analysis and Modeling of Flow in Rotating Spiral Microchannels:

Towards Math-Aided Design of Microfluidic Systems Using Centrifugal Pumping," Lab on a Chip, 11(12), pp. 2097-2108.
[45] Chang, H. C., Tsou, C., Lai, C. C., and Wun, G. H., 2008, "A Real-Time Dynamic Imaging System for Centrifugal Microflow Platforms," Measurement Science and Technology, 19(7), pp. 075501.
[46] Kim, N., Dempsey, C. M., Zoval, J. V., Sze, J. Y., and Madou, M. J., 2007, "Automated Microfluidic Compact Disc (Cd) Cultivation System of *Caenorhabditis Elegans*," Sensors and Actuators B: Chemical, 122(2), pp. 511-518.
[47] Watts, A. S., Urbas, A. A., Moschou, E., Gavalas, V. G., Zoval, J. V., Madou, M., and Bachas, L. G., 2007, "Centrifugal Microfluidics with Integrated Sensing Microdome Optodes for Multiion Detection," Analytical Chemistry, 79(21), pp. 8046-8054.
[48] Puckett, L. G., Dikici, E., Lai, S., Madou, M., Bachas, L. G., and Daunert, S., 2004, "Investigation into the Applicability of the Centrifugal Microfluidics Platform for the Development of Protein-Ligand Binding Assays Incorporating Enhanced Green Fluorescent Protein as a Fluorescent Reporter," Analytical Chemistry, 76(24), pp. 7263-7268.
[49] Lai, S., Wang, S., Luo, J., Lee, L. J., Yang, S. T., and Madou, M. J., 2004, "Design of a Compact Disk-Like Microfluidic Platform for Enzyme-Linked Immunosorbent Assay," Analytical Chemistry, 76(7), pp. 1832-1837.

Appendix A

Table 1. Selected literature for application of centrifugal microfluidics

Reference	Geometry	Range of rotational speed	Area of investigation	Nature of work
Ukita et al. [36]	Detection reservoir volume = 2.8 μl, depth = 700 μm	0-2000 RPM	Multifunctional capillary bundle structures for immunoassay	Experimental
Kong et al.[27]	Chamber radius = 4 mm Chamber depth = 1.4 mm	450-1580 RPM	Pneumatic agitation on continually rotating microfluidic platform	Experimental
Kong et al. [34]	Chamber diameter = 6.35 mm Chamber depth = 1.4 mm Liquid volume = 68 μL	400-1200 RPM	Pneumatic flow switching on centrifugal microfluidic platform	Experimental
Gorkin et al. [37]	d_r = 2. 3-12.55 mm	0-6000 RPM	Suction enhanced siphon valves	Experimental and analytical
Burger et al. [38]	a = 100 μm, b = 25 μm	250-3000 RPM	Cell handling : separation and capturing/counting	Experimental
Chakraborty et al. [26]	T-microchannel a = 1 mm, b = 100 μm, L = 3.6 cm, d_r = 2.2 cm	~100-4500 RPM	Investigation of anomalous mixing behavior in rotating microchannels	Analytical and experimental
Burger et al. [39]	-	3 – 30 Hz	Infrared thermo-cycler with direct on disk wireless temperature measurement system	Experimental
Moore et al. [40]	Reservoir depth = 1 mm Valve channel dimensions a = 127, 254, 508 μm b = 254, 508, 762, 1016 μm	160-560 RPM	Behavior of capillary valves prepared by three-dimensional (solid-object) printing	Experimental
Kong et al. [41]	Capillary diameter = 75 μm	0-2600 RPM	A valveless pneumatic fluid transfer technique	Experimental
Abi-Samra et al. [42]	a = 1 mm, b = 100 μm	300-1200 RPM	Thermo-pneumatic pumping	Analytical and experimental
Mark et al. [43]	a = 400 μm, b = 200 μm	10-28 Hz Rate: 1.7 Hz/s	Aliquoting based on centrifuge-pneumatic valve	Experimental and numerical
Amasia et al. [35]	-	0-2000 RPM	PCR amplification using integrated thermo-electric heating and ice-valving	Experimental
Wang et al. [44]	d_r = 1. 9 cm (i) a = 90 μm, b = 33 μm (ii) a = 50 μm, b = 25 μm	1400-2400 RPM	Analysis and modeling of flow in rotating spiral microchannels	Analytical, numerical and experimental
Siegrist et al. [7]	Microchamber area = 75-250 mm^2 b = 200 μm	0-2000 RPM	Uniform microchamber filling behavior	Numerical and experimental
Noroozi et al. [23]	Three 240 μm-deep reservoirs, one 60 μm-deep mixing chamber, a = 60 μm, b = 240 μm	Rotating frequency = 0-24 Hz	Reciprocating flow based centrifugal microfluidics mixer	Experimental
Chakraborty et al.[19]	d_r = 2.197 cm a = 100 μm, b = 1 mm	200-700 RPM	Capillary filling with dynamically evolving contact line motion	Analytical, numerical and experi mental

Chang et al. [45]	a = 300 μm, b = 200 μm microvalve dimensions: D_h = 5 mm, b = 400 μm	0-4500 RPM	Real-time dynamic imaging system	Experimental
Liu et al. [21]	d_r = 2. 6 cm, L = 1.0cm	140-170 rad/s	Modeling of flow field, flow burst and flow timing	Analytical
Chen et al. [30]	d_r (reservoir)=2.70 cm d_r (valve)= 3.15 cm a = 300 and 400 μm b = 8-600 μm Valve expansion angle = 30° - 100°	100-1000 RPM	Analysis and experiment of capillary burst valves on a rotating disk	Analytical and experimental
Kim et al. [46]	Components: a nutrient reservoir, a cultivation chamber and a waste reservoir. a = 50 μm, b = 40 μm	~227-1726 RPM Acceleration = ~17-980 m/s^2	Cultivation of *Caenorhabditis elegans* in microfluidic compact disk system	Experimental
Cho et al. [28]	d_r = 2.75 cm, a = 15-150 μm, b = 150 μm Valve expansion angle = 60°, 90°, 120°	~0-3000 RPM	Working principle of capillary burst valve	Analytical and experimental
Watts et al. [47]	a = 250-500 μm b = 200 μm	Burst frequency ~ 500-960 RPM	Multi-ion detection (Na, K, Ca, Cl) using integrated sensing microdome optodes	Experimental
Kim et al. [32]	D_h = 80 μm, a = 215 μm Δr = 1.35 cm	40-120 rad/s	Passive flow switching valves	Analytical and Experimental
Kido et al. [25]	Microchamber volume = 70 μL	50-7000 RPM	Cell lysis and sample homogenization	Experimental
Ducree et al. [16]	(i)a=100 μm, b=100 μm (ii) a=1265 μm, b=60 μm L = 2.1 cm	50-300 rad/s	Multilamination of flows in planar networks	Numerical and experimental
Ducree et al. [6]	d_r = 2.0-3.0 cm L = 2.0-2.1 cm a = 100-500 μm, b = 65-100 μm	0-150 Hz	Patterning and mixing in rotating radial microchannel	Analytical, numerical and experimental
Grumann et al. [22]	d_r = 3.9 cm mixing chamber diameter = 6 mm	~5-8 Hz	Batch-mode mixing on centrifugal microfluidic platform	Experimental
Puckett et al. [48]	Three burst valves used (i) a=635 μm , b=635 μm (ii) & (iii) a = 127 μm, b = 63.5 μm	0-1050 RPM Ramping speed = 30 RPM/s	Development of protein-ligand binding assays	Experimental
Brenner et al. [33]	a = 360 μm, b = 125 μm L = 10.1 mm	75-350 rad/s	Frequency dependent transversal flow control	Analytical and Experimental
Lai et al. [49]	a = 127-762 μm, b = 60-800 μm	360-1280 RPM	Enzyme-linked immunosorbent assay	Experimental
Madou et al. [18]	(i) a=127 μm, b=63.5 μm (ii) a=254 μm, b=127 μm (iii) a=508 μm, b=254 μm	Burst frequency ~ 524-1126 RPM	Design of a polymer based microfluidic compact disk platform	Experimental
Zeng et al. [5]	D_h = 36-250 μm	Critical burst condition, $\rho\omega^2 r\Delta r$ = 0-5000 Pa	Design analyses of capillary burst valves	Numerical and experimental
Duffy et al. [17]	D_h = 5 μm–0.5 mm b = 16 μm–3 mm	60-3000 RPM	Characterization and multiple enzymatic assays	Experimental

Available online at www.sciencedirect.com

SciVerse ScienceDirect

Procedia Engineering 00 (2012) 000–000

Procedia Engineering

www.elsevier.com/locate/procedia

5th BSME International Conference on Thermal Engineering

Heterogeneous Structure in Diesel Fuel Sprays

Hironobu Ueki[a]*

[a]*Nagasaki University, 1-14 Bunkyo-machi, Nagasaki 852-8521, Japan*

Abstract

A laser 2-focus velocimeter (L2F) has been applied for measurements of velocity and size of droplets in diesel sprays. The maximum data acquisition rate of 15 MHz has been achieved by using FPGA in order to capture every droplet which appears in the micro-scale measurement volume. A method of evaluating the mass flow rate of droplets was proposed, and the distance between droplets was adopted as an indicator of the number density of droplets and the heterogeneous structure of sprays. The diesel fuel spray was injected intermittently into the atmosphere by using a 5-hole injector nozzle. The orifice diameter of the injector nozzle was 0.113 mm, and the injection pressure was set at 40MPa by using a common rail system. Measurements were conducted in the spray on 10 planes from 5 to 25 mm downstream from the nozzle exit. It was shown that the velocity of droplet was the highest at the spray center and decreased towards the spray periphery. The size of droplet at the spray center decreased downstream and that at spray periphery increased downstream. The mass flow rate near the spray center was larger than that in the spray periphery region. It was confirmed that the fuel mass per injection evaluated by the proposed method based on the L2F measurement was nearly equal to the injected mass in a plane further than 15 mm from the nozzle exit. The probability density of droplet with a distance shorter than 5 μm to the adjacent droplet increased remarkably near the spray center 5 and 12 mm downstream from the nozzle exit. It is thought that a region of high number density of droplet exists at the spray center near the spray tip when the spray penetration is shorter than 15 mm.

Keywords: Heat Engine, Droplet, Atomization, Laser Measurement

Nomenclature

d	Diameter of nozzle orifice (mm)
F	Focus diameter (μm)
L	Focus length (μm)
S	Distance between two foci (μm)
T	Time after injection start (ms)
t_1	Time-of-flight (ms)
t_2	Time-of-scattering on the upstream focus (ms)
t_3	Time-of-scattering on the downstream focus (ms)
t	Time (ms)
u	Velocity (m/s)
d_p	Diameter of droplet (μm)
L_d	Distance between droplets (μm)
A	Area (mm^2)
m_f	Mass flow rate

* Corresponding author. Tel.: +81-95-819-2520; fax: +81-95-819-2534.
E-mail address: ueki@nagasaki-u.ac.jp

M	Injected mass (mg/cycle)
N_v	Number of valid data
N_a	Number of all data
x	Coordinate (mm)
y	Coordinate (mm)
z	Coordinate (mm)

1. Introduction

Not only the reduction of exhaust emissions but also further improvement of thermal efficiency is required to diesel engines. As appropriate control of combustion is necessary to meet these requirements, it is important to understand the influence of fuel spray characteristics upon the diesel combustion. Many researchers have investigated about the relation between the injection condition and combustion. For example, the effect of injection pressure on soot formation was reported by Crua, et al. [1]. It has been reported that the high speed fuel spray injected by microscopic hole was effective for further improvement of combustion [6]. Research work is also needed for basic understanding of the spray characteristics. Image processing [7], PDPA [8] and ILIDS [2] are effective as measurement methods of velocity and size of spray droplets. Especially, the information of spray behavior near the nozzle orifice is indispensable for designing the nozzle shape, modeling droplet disintegration and setting the initial condition of simulating droplet disintegration [9,10]. The spatial distribution of the mass in the near-nozzle region was measured by the X- ray radiography technique [3]. There are few studies of the inner structure of the spray where the droplet number density is high.

A laser 2-focus velocimeter (L2F) can measure the time-of-flight when a droplet flies between two foci and gives us the velocity. L2F has the high optical signal to noise ratio, so the influence of multiple scattering on the spray measurement is small. Schodl [11] reported about the application of L2F to the internal flow of turbomachinery in 1974. It was reported by Chaves [12] and Shugger [13] that measurement systems similar to the L2F were successfully applied to measure droplets which were located inside the breakup length. The authors showed that the simultaneous measurements of the velocity and size of droplets were possible by adding the measurement of time-of-scattering to L2F [14].

In the present study, a method of evaluating the mass flow rate of droplets was proposed, and the distance between droplets was adopted as an indicator of the number density of droplets and the heterogeneous structure of sprays. The diesel fuel spray was injected intermittently into the atmosphere by using a 5-hole injector nozzle. The velocity and size of droplets in the spray have been measured by the L2F on 10 planes 5 to 25 mm from the nozzle exit. The spatial distributions of velocity, size, and mass flow rate of droplets have been evaluated, and the region of high number density of droplets has been investigated.

2. Experimental Setup

2.1. Advanced Laser 2-Focus Velocimeter; L2F

The light probe of the L2F consists of highly focused two laser beams as shown in Fig.1. The diameter F of the focus is about 3μm, and the distance S between two foci is 17μm, and the length L is about 20μm in the direction of optical axis. It can be mentioned that the L2F used in the present study has a micro-scale probe. The measurements of time-of-flight and time-of-scattering are shown in Fig.2. The upper half of Fig.2 shows the cross-section of the L2F probe. When a droplet flies through both upstream and downstream foci, time-of-flight t_1, time-of-scattering t_2 on the upstream focus and time-of-scattering t_3 on the downstream focus are measured by a digital counter. The velocity of a droplet can be easily calculated by dividing the distance between two foci S with the measured time-of-flight t_1, that is

$$u = \frac{S}{t_1} \tag{1}$$

The relation used for the estimation of droplet size is that the ratio of the time-of-flight and the time-of-scattering corresponds to the ratio of the distance between two foci S and the droplet size d_p plus the focus size F. The time-of-scattering can be estimated by averaging two time-of-scattering. The droplet size d_p can be estimated by

$$d_p = u \cdot \frac{(t_2 + t_3)}{2} - F \tag{2}$$

The L2F selects a droplet which passes through the upstream focus and downstream focus sequentially. The time-of-fight is shortest when a single droplet passes through two foci, and the time-of-flight is longer when two different droplets pass through two foci. So, a velocity given by different droplets is overestimated and can be removed by a statistical analysis. When the number density of droplet is very high, the local droplet distance is sometimes shorter than the distance between

two foci. In such a case, the droplet other than the droplet which passed the upstream focus will pass the downstream focus. Then, the time-of-flight is not measured correctly. When the flight direction of a droplet is fluctuating, the droplet which passes the upstream focus sometimes differs from the droplet which passes the downstream focus. The velocity obtained by such a pair of different droplets should not be correct. Figure 3 shows the flowchart of the measurements of the time-of-flight and time-of-scattering. Counting starts by the detection of an upstream signal and stops by the detection of a downstream signal, and an up-and-down flag is saved with a counted value. When an upstream signal is detected before detecting a downstream signal, an up-and-up flag is saved with counted value. Valid data can be selected by checking the flag. The sampling data number N_a, which corresponds to the number of the droplets passing through the upstream focus, is set before the measurement.

Figure 4 shows the system configuration of the L2F. The light source is a semiconductor laser which has a maximum power of 100mW and a wave length of 835 nm. A non-spherical lens which has a focal length of 8 mm and a numerical

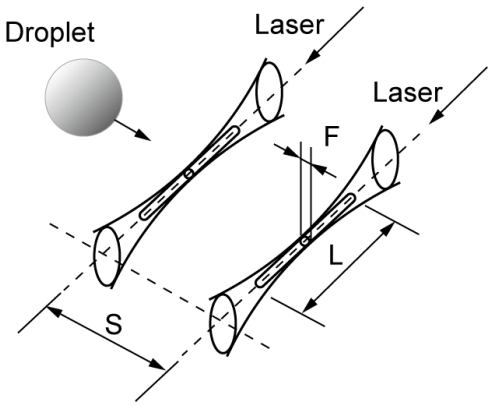

Fig. 1. Light probe of L2F.

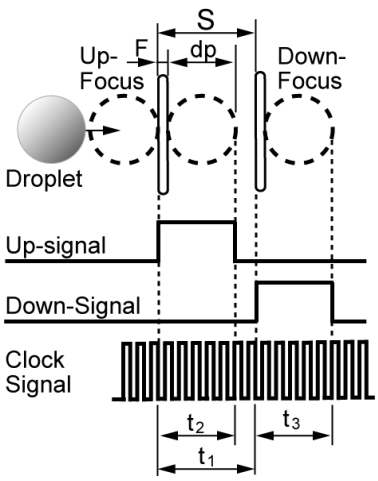

Fig. 2. Time-of-flight and time-of-scattering.

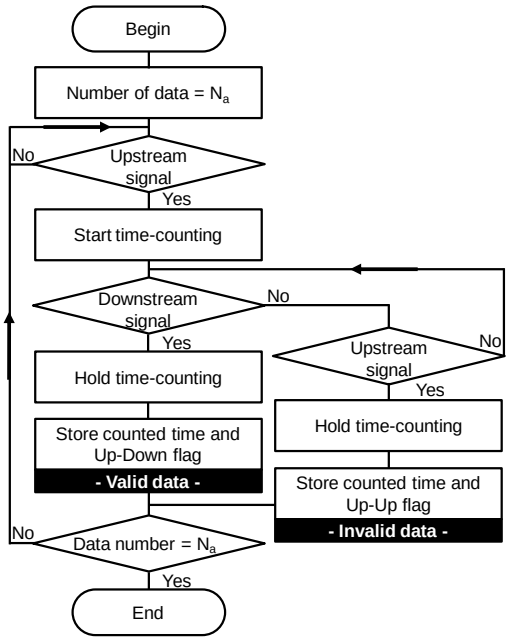

Fig. 3. Flowchart of data acquisition procedure.

aperture of 0.5 is adopted as the condensing lens. By the optical system with a length of 350 mm including the light source, the backscattering light of a droplet at the focus is guided to a Si- APD (Silicon Avalanche Photo Diode), and it is converted into an electrical signal. The time-of-flight and time-of-scattering are measured by the digital counter which is mainly constituted by a FPGA (Field Programmable Gateway Array) with a clock of 160MHz. The maximum data sampling rate of the L2F system is set at 15MHz.

A preliminary experiment has been conducted to confirm the accuracy of size measurement. Droplets generated by a humidifier were seeded in the air flow of about 50 m/s in velocity and they were measured by L2F and PDA (PDI-200MD manufactured by Artium) simultaneously. Figure 5 shows the comparison between probability density distributions of mass-based droplet size measured by L2F and PDA. It is understood that two probability density distributions are very close to each other. The mass-based arithmetic mean sizes measured by L2F and PDA are 9.2 and 9.5 μm respectively. The error in size measurement was 3%. It is understood that the error in mass evaluation is small.

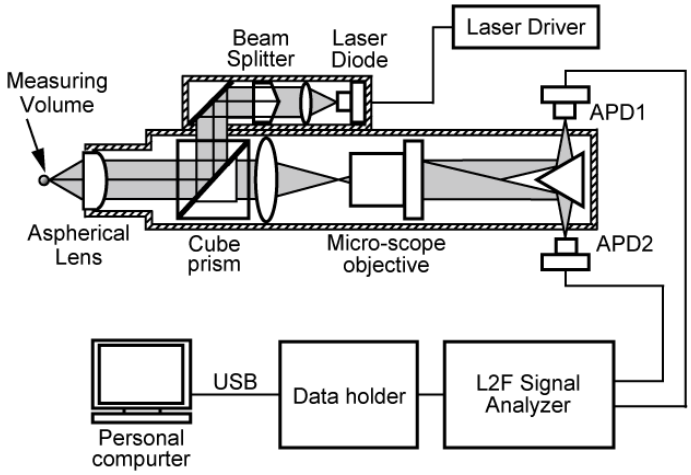

Fig. 4. System diagram of L2F.

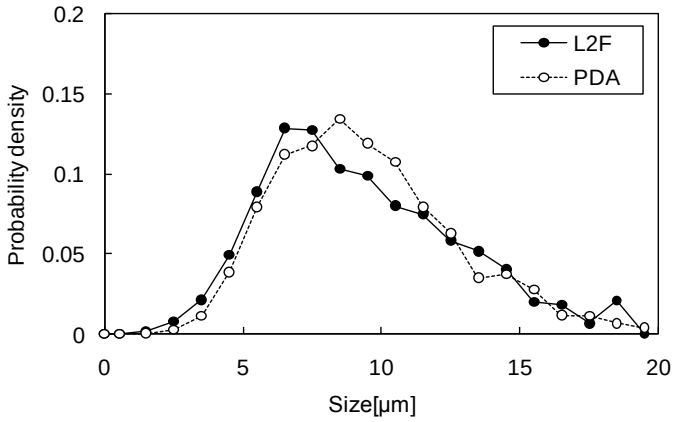

Fig. 5. Probability density distributions of mass-based droplet size measured by L2F and PDA.

2.2. Fuel Spray Measurement System

A common rail injector was used to control injection conditions, such as the injection timing, injection duration and injection pressure. Figure 6 is the measurement system of fuel sprays using the L2F. Diesel fuel pressurized by the high pressure pump was stored in the rail. The rail pressure was set at 40MPa. The fuel was injected intermittently into the atmosphere at a temperature of 298±6K and a pressure of 0.1MPa. The test nozzle was a 5-hole injector with a hole diameter d of 0.113 mm. The measurement of the spray was conducted within one of 5 spray plumes while the remaining 4 plumes were shielded and sucked out through small pipes. The injection interval was 330 ms. The period of energizing the solenoid was 1.0 ms, and the injection period was 0.79 ms. The fuel of 1.34 mg was injected per cycle from one hole. A clock signal with a frequency of 6MHz was used for recording the time when the L2F data was acquired. The number of data N_a was 10,000 at each measurement position. The coordinate z is the distance along the spray axis from the nozzle tip, the coordinate y is the distance along the laser axis, and the coordinate x is perpendicular to y z-axis. The x-axis indicates the radius from the spray center on the plane $y = 0$. Figure 7 shows a spray photograph and measurement positions. There is a dark domain near the position of $z = 5$ mm. This is the shadow of the plug to shield 4 plumes. Simultaneous measurements of velocity and size of spray droplets were conducted on planes perpendicular to z-axis; z = 5, 9, 10, 11, 12, 13, 14, 15, 20 and 25 mm. The table 1 shows the x-coordinates of measurement positions in each z plane. The y-coordinates of the measurement positions were fixed to zero. The measurement data were accumulated during 100-1200 injections. In each z plane, $x = 0$ mm corresponds to the spray center, and the most outside measurement position is called the spray periphery.

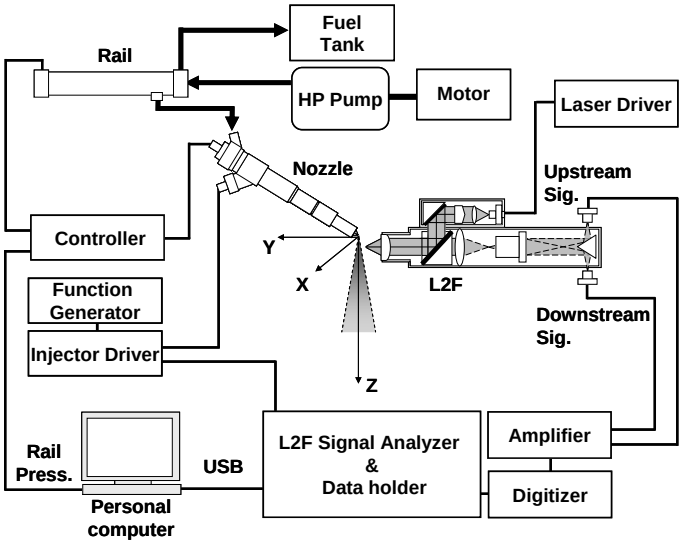

Fig. 6. Fuel spray measurement system.

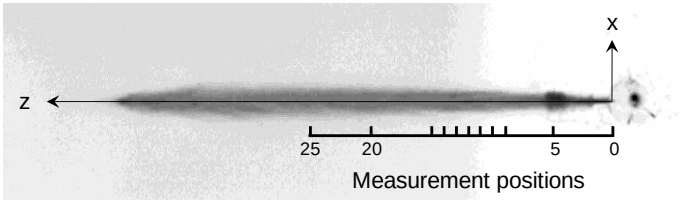

Fig. 7. Spray image and measurement positions (z = 5, 9, 10, 11, 12, 13, 14, 15, 20, 25 mm).

Table 1. Measurement positions.

z(mm)	x(mm)
5	0, ±0.1, ±0.2, ±0.3, ±0.4, ±0.5, ±0.6, ±0.7, ±0.8
9	0, ±0.2, ±0.4, ±0.6, ±0.8, ±1.0
10	0, ±0.2, ±0.4, ±0.6, ±0.8, ±1.0
11	0, ±0.2, ±0.4, ±0.6, ±0.8, ±1.0
12	0, ±0.2, ±0.4, ±0.6, ±0.8, ±1.0
13	0, ±0.2, ±0.4, ±0.6, ±0.8, ±1.0, ±1.2
14	0, ±0.2, ±0.4, ±0.6, ±0.8, ±1.0, ±1.2
15	0, ±0.3, ±0.6, ±0.9, ±1.2
20	0, ±0.4, ±0.8, ±1.2, ±1.6
25	0, ±0.5, ±1.0, ±1.5, ±2.0

2.3. Evaluation of Number Density and Mass Flow Rate

Spatial distribution of droplets is very important for understanding the spray characteristics in a region of high number density droplets and for understanding the processes of evaporation and combustion. A distance L_d between droplets along the direction from upstream focus to downstream focus can be estimated by,

$$L_d = u \cdot \Delta T \tag{3}$$

where ΔT is a time interval between droplet observations and u is an instantaneous velocity.

An important step towards understanding the spray behavior is to estimate the mass flow rate during injection. The mass flow rate is the total mass of droplets passing the measurement probe in a certain time. The mass flow rate m_f estimated as

$$m_f(x,T) = \frac{\rho \cdot \sum V_p(x,T)}{\sum \left(\Delta t(x,T) \cdot \left(L + d_p(x,T)\right) \cdot \left(F + d_p(x,T)\right)\right)} \tag{4}$$

where d_p is the size of droplet, and V_p is the volume of droplet. The total mass M of a single injection can be estimated by the integral of mass flow rate with time and space. When an axisymmetric spray is assumed,

$$M(x,T) = \sum_x \sum_t m_f(x,T) \Delta A(x) \Delta T \tag{5}$$

where ΔA is the cross section of a ring of width Δx which is the distance between the x-coordinate of the measurement positions. The cross section is calculated by

$$\Delta A(x) = 2\pi x \Delta x \tag{6}$$

As shown in Table 1, Δx depends on z. For example, Δx = 0.1 mm in the plane of z = 5 mm. The spray edge was decided on x = ±0.8 mm based on spray images. This was confirmed by the fact that a droplet was not detected at x = ±0.9 mm.

3. Results and Discussion

3.1. Temporal and Spatial Changes in Velocity and Size of Droplets

Figure 8(a) shows the time variation of the mean droplet velocity at 5 positions on the plane z = 5 mm. The mean velocity at the spray center was about 100 m/s at the time T = 0.8 ms, and this is on the same order of magnitude as measured from the spray image. At the points x = 0 mm and x = ±0.4 mm, the mean velocity increased in a period between 0.8 ms and 1.2 ms, and the change in velocity was relatively small in a period between 1.2 and 1.5 ms. The mean velocity decreased rapidly after 1.5 ms and the period after the start of velocity decrease is called period II in this paper. The period before period II is called period I. The period I and period II correspond to so called spray head and spray tail respectively. At the points x = ±0.8 mm, the velocity decreased gradually in a period between 1.0 ms and 1.5 ms. The mean velocities at two measurement positions with the same distance from the spray center, for example x = -1.5 mm and x = 1.5 mm, were nearly the same. Figure 8(b) shows the time variation of the mean droplet velocity at 5 positions on the plane z = 25 mm. The mean velocity at the spray center was about 140 m/s at 1.0 ms. This velocity agreed well with the one which was estimated from the spray images. Droplets appeared at 1.0 ms at the points x = 0, and ±0.5 mm. And they appeared at 1.1 ms at the point x = ±1.5 mm. It is understood that droplets near the spray center reached the measurement position earlier than the droplets in the periphery region. At the positions x = 0 mm and x = ±0.5 mm, the mean velocity increased in a period between 1.0 and 1.2 ms, and the change in velocity was relatively small in a period between 1.2 and 1.5 ms.

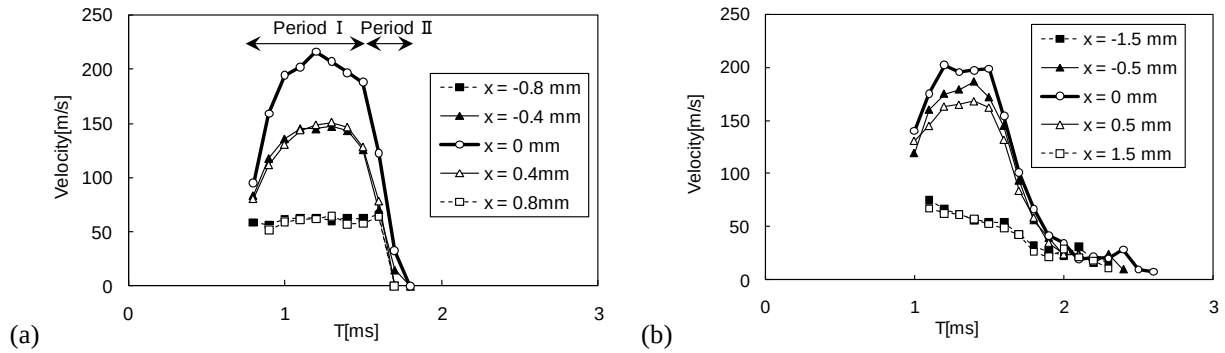

Fig. 8. Time change in Arithmetic mean velocity for (a) z = 5 mm and (b) z = 25 mm.

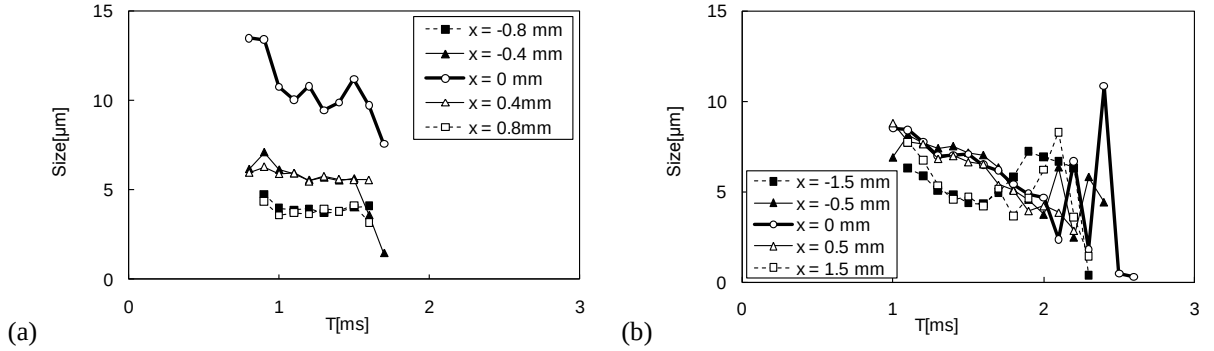

Fig. 9. Time change in Arithmetic mean size for (a) z = 5 mm and (b) z = 25 mm.

Figure 9(a) shows the time variation of the arithmetic mean droplet size on the plane z=5 mm. The mean droplet size when the spray tip reached the measurement position was the largest in the period between 1.0 and 1.5 ms, and the droplet size gradually decreased at every measurement position. Figure 9(b) shows the time variation of the mean droplet size on the plane z=25 mm. The mean droplet size gradually decreased at every measurement position in the first half of the injection duration. The size fluctuated in the latter half of the injection duration.

The time interval between droplets was estimated from the time of droplet observation. Figure 10(a) shows the time variation of the mean time interval within each time window of 0.1 ms on the plane z=5 mm. The time interval at the position x = 0 mm increased in the first half of the injection duration and decreased after that. At positions x = ±0.4 mm, the time interval was shorter than 50 μs during the injection period. At positions x = ±0.8 mm, the time interval decreased in the first half of the injection duration and increased after that. Figure 10(b) shows the time variation of the mean time interval on the plane z=25 mm. At positions x = 0 mm and x = ±0.5 mm, the time interval was between 15 and 50μs in the first half of the injection duration and increased after 1.6 ms. At positions x = ±1.5 mm, the mean time interval decreased in the period between 1.1 ms and 1.3 ms, and increased after 1.3 ms. The time interval between droplets in the spray periphery region was longer than the one at the spray center during the injection period.

The velocity and size in the Period I were used for calculating the mean values at each measurement position, because the temporal change was relatively small. Figure 11(a) shows spatial distributions of the mean velocity on planes z = 5, 10, 15, 20 and 25 mm. The mean velocity showed the highest near the spray center and decreased towards the periphery region. It is understood that the spatial distribution of the mean velocity of droplet is nearly axisymmetry. Figure 11(b) shows the spatial distributions of the arithmetic mean size. On every plane z = constant, it can be seen that the spatial distribution of mean size was nearly axisymmetric as for the one of mean velocity. The mean size showed the largest near the spray center and decreased gradually with the distance from the spray axis towards the periphery region on the plane z = 5 mm. An

increase in size was observed near the spray periphery on planes further than 5 mm from the nozzle exit. Yeh et. al. [4] reported a similar droplet size distribution. It is also understood that the mean size decreased along the spray axis from z = 5 to z = 15 mm.

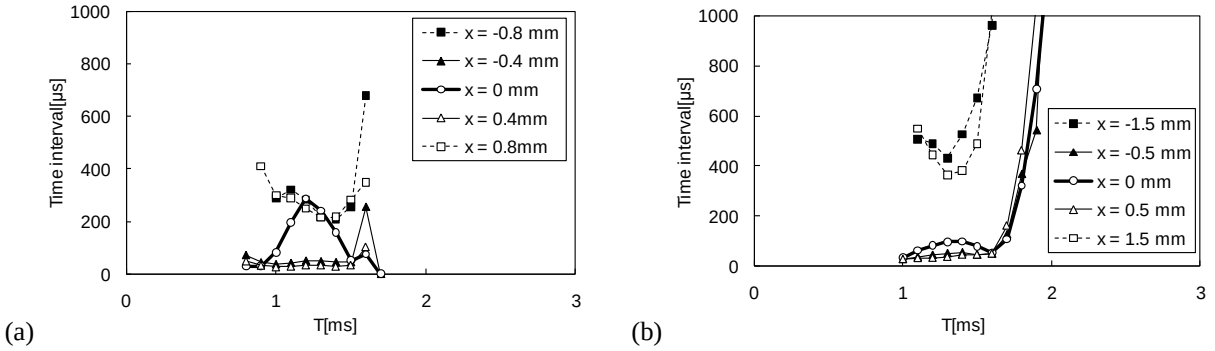

Fig. 10. Time change in Arithmetic mean time interval for (a) z = 5 mm and (b) z = 25 mm.

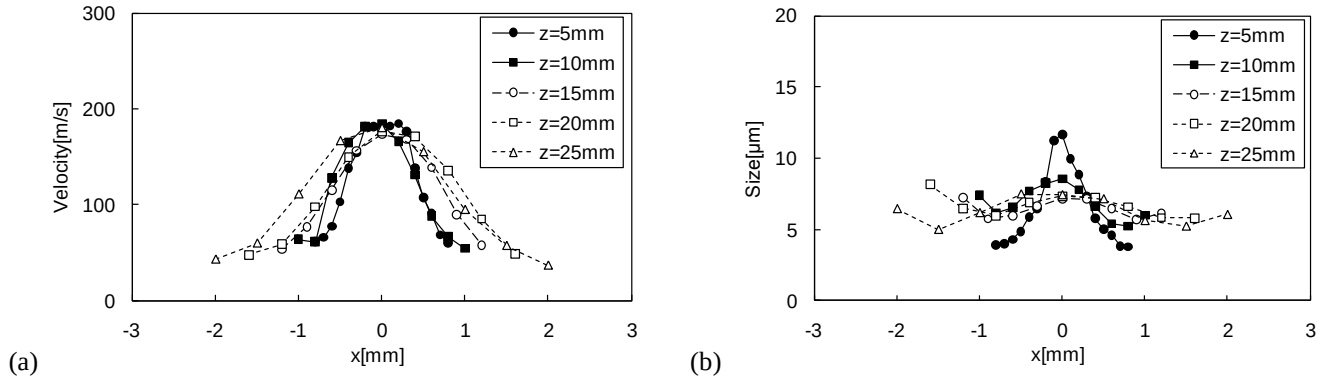

Fig. 11. Spatial distribution in the period I for (a) velocity and (b) size.

3.2. Estimation of Mass Flow Rate

Values of V, d_p and ΔT in the Eqn. (4) for estimating the mass flow rate are given by droplets which passed both upstream and downstream foci. In order to evaluate the mass flow rate of all droplets which passes the measurement volume, it is needed to additionally evaluate the mass of droplets which passed only the upstream focus. Figure 2 shows the ratio of N_v and N_a at each measurement positions on planes z = 5 to 25 mm. The ratio of N_v / N_a was higher than 0.5 near the spray center, although, it decreased to about 0.1 in the spray periphery region. The decrease in the valid data ratio comes mainly from different droplets passing through two foci due to the fluctuation in the direction of droplet flight. The relation between the valid data ratio and the fluctuation of flight direction has been investigated theoretically by Hayami [5]. It was shown that the valid data rate could be estimated to be about 50% when the fluctuation of flight direction was 10 degrees. Therefore, the value of N_v / N_a was thought to be appropriate.

The total mass of droplets passing through the measurement volume is the summation of the mass of droplets passing through both upstream and downstream foci and the mass of droplets passing through only upstream focus. As droplets randomly pass through the measurement volume, it is expected that the mass of droplets is proportional to the number of observed droplets. Accordingly, the mass flow rate of droplets was estimated from the one evaluated by the Eqn. (4) multiplied by N_a / N_v. Figure 13 shows the spatial distribution of the mass flow rate on the plane z = 25 mm within each time window of 0.2 ms. The mass flow rate near the spray center was higher than the one of the spray periphery at each time. The

distribution of mass flow rate can be calculated by integrating time dependent distributions shown in Fig. 13. Figure 14 shows the spatial distribution of mass flow rate on planes z = 5, 10, 15, 20 and 25 mm. It can be seen that the spatial distribution of mass flow rate was nearly axisymmetric. The mass flow rate at the center was the highest at the plane z = 5 mm, and decreased toward the downstream. A peak was not seen on the planes z = 15 - 25 mm, and higher mass flow rates were distributed between positions x = ±0.5 mm.

The fuel mass injected within a single injection can be evaluated by the Eqn. (5). The mass evaluated by the L2F was 1.47mg/injection. As the weighed mass was 1.34mg/injection, the ratio of the evaluated mass and the weighed mass was about 1.1. The error in the evaluation would come from the assumption that the spray is axisymmetric and that the droplet is a sphere. Figure 15 shows the ratio of the evaluated mass and the weighed mass at each measurement position. On measurement planes downstream from the plane z = 15 mm, the ratio of the evaluated mass and the weighed mass was about 1.0. It is understood that almost all droplets were identified by the L2F properly. However, the evaluated mass decreased to less than 1.0 on the planes nearer to the nozzle exit than z = 15 mm. It is understood that unidentified mass increases near the nozzle.

In order to identify the region of high number density of droplets, the distance between surfaces of droplets was estimated by subtracting the droplet size from the distance L_d. Figure 16 shows probability density distribution of the distance between surfaces of droplets at the spray center on planes of z =5, 12, 15, 20 and 25 mm. The probability density of the distance shorter than 20μm on planes z = 5 and 12 mm was higher than that on planes z = 15, 20 and 25 mm. Short distance between droplets means that the number density of droplets is high. It is thought that the laser beam might be scattered by high number density droplets and could not penetrate into the spray center on planes z = 5 and 12 mm. Underestimation of the fuel mass near the nozzle exit should be due to high number density droplets.

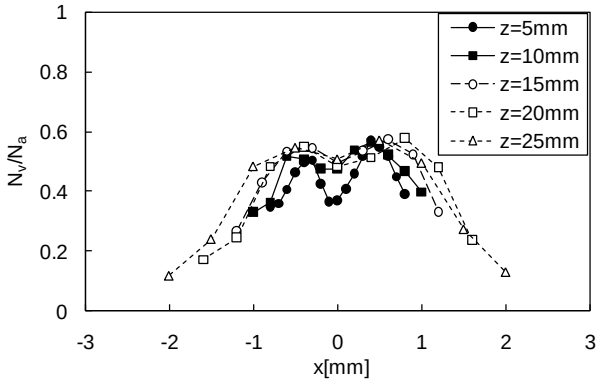

Fig. 12. Ratio of valid data number and all data number; Period I.

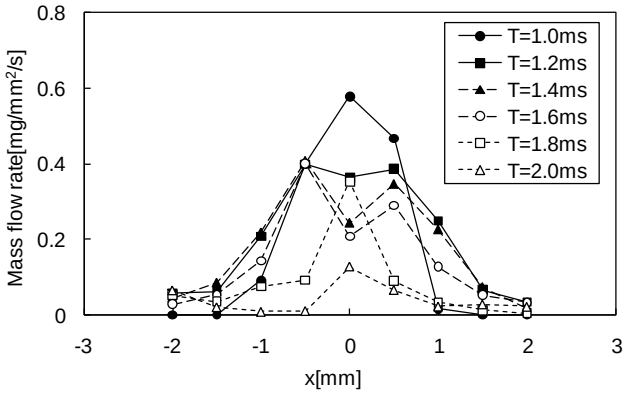

Fig. 13. Spatial distribution of mass flow rate; z = 25 mm.

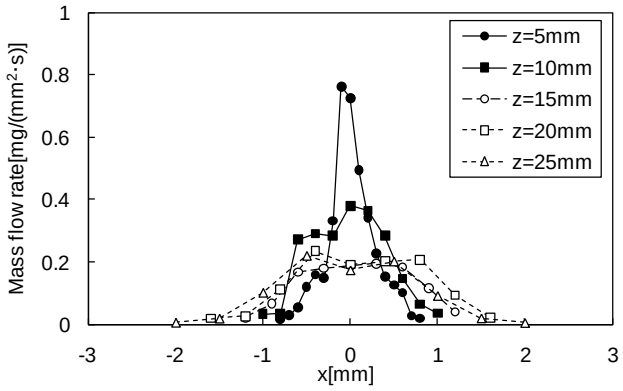

Fig. 14. Spatial distribution of mass flow rate.

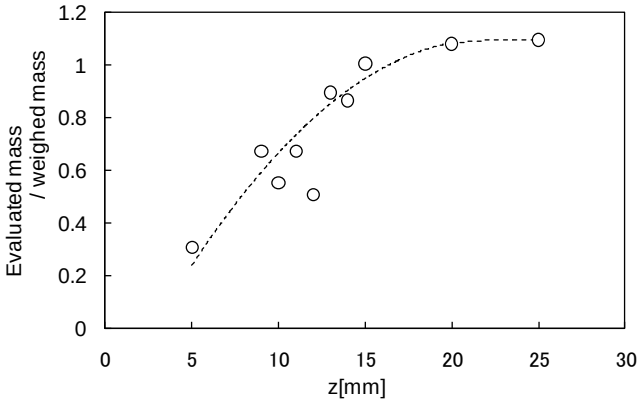

Fig. 15. Ratio of evaluated mass per injected mass.

Figure 17(a) shows the probability density distribution of the distance between surfaces of droplets at 5 positions x = 0.0,0.1, 0.2, 0.3 and 0.4 mm on the plane z = 5 mm. It is clearly seen that the probability density of the distance shorter than 20μm at the position x = 0.0 mm was higher than that at positions x = 0.1, 0.2, and 0.4 mm. It is thought that a region of high number density of droplets exists inside of the position x = 0.1 mm. That is, the diameter of the high number density region can be thought as an order of 0.1 mm on z = 5 mm. Figure 17(b) shows the probability density distribution of the distance between surfaces of droplets at 4 positions x = 0.0, 0.2, 0.4 and 0.6 mm on the plane z = 12 mm. The probability densities of the distance shorter than 10μm at positions x = 0.0 and 0.2 mm were relatively higher than that at positions x = 0.4 and 0.6 mm. Figure 18 shows the time variation of the probability density of droplets with a distance between their surfaces shorter than 5μm at the spray center on planes z = 5 and 12 mm. It is understood that the region of high number density of droplet appeared at the time when the spray tip reached the measurement position. In other words, a region of high number density of droplets is thought to exist at the spray center near the spray tip when the spray penetration is shorter than 15 mm.

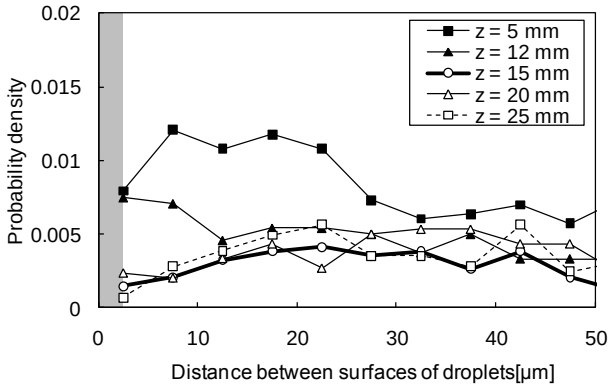

Fig. 16. Probability density of distance between surfaces of adjacent droplets ; x=0 mm.

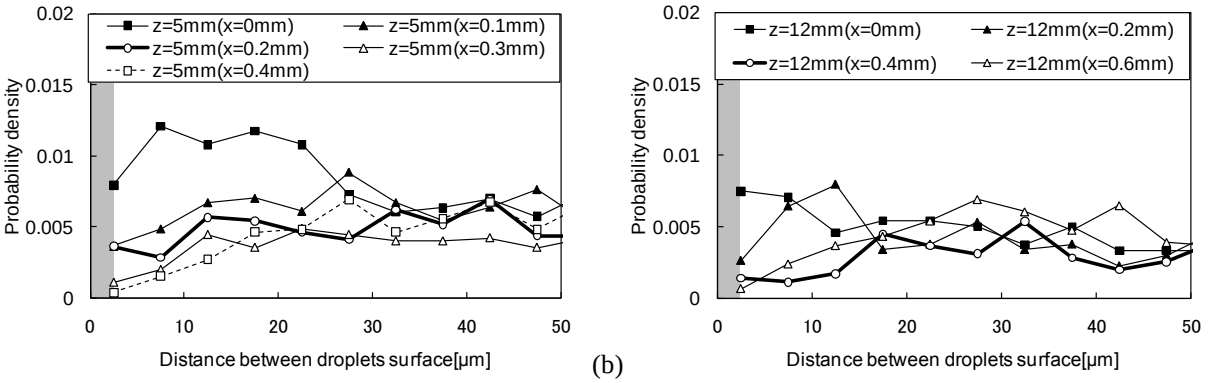

Fig. 17. Probability density of distance between surfaces of adjacent droplets for (a) z = 5 mm and (b) z = 25 mm.

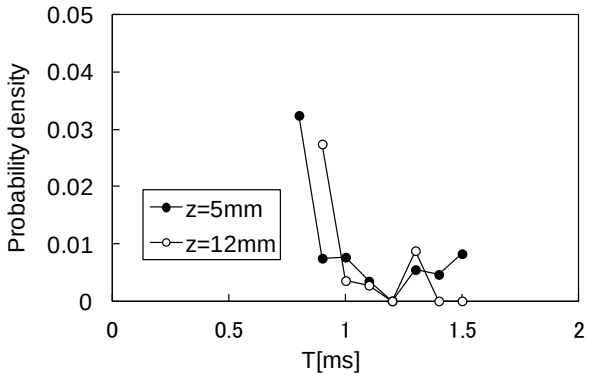

Fig. 18. Probability density of droplets with a distance between their surfaces shorter than 5μm at the spray center.

4. Conclusions

A L2F has been utilized for measurements of velocity and size of droplets in diesel fuel sprays injected under a common rail pressure of 40MPa. A method of evaluating the mass flow rate of droplets was proposed, and the distance between droplets was adopted as an indicator of the number density of droplets and the heterogeneous structure of sprays. Measurements were conducted inside sprays on 10 planes from 5 to 25mm downstream from the nozzle exit. Based on the measurement of temporal changes in velocity and size of droplets, mean values of velocity and size at each measurement position were evaluated. The results showed that the velocity of droplet was the highest at the spray center and decreased towards the spray periphery. The size of droplet at the spray center decreased downstream and that at spray periphery increased downstream. The mass flow rate near the spray center was larger than that in the spray periphery region. The fuel mass per injection evaluated by the proposed method based on the L2F measurement was nearly equal to the weighed mass on planes further than 15 mm from the nozzle exit. It is thought that a region of high number density of droplet exists at the spray center near the spray tip when the spray penetration is shorter than 15 mm. The effect of injection conditions such as the injection pressure, ambient pressure, and nozzle hole diameter on the heterogeneous structure of sprays will be investigated in a future work.

References

- Journal articles:

[1] Crua, C., Kennaird, D.A., Heikal, M.R., 2003. Laser-induced incandescence study of diesel soot formation in a rapid compression machine at elevated pressures, Combustion and Flame, 135(4), pp.475-488

[2] Ryu, C-S., Moriyoshi, Y., Aoyanagi, Y., 2007. 2D Simultaneous Measurements of Droplets Diameter and Velocity in a Diesel Spray by Using Improved ILIDS Method, Transactions of the Japan Society of Mechanical Engineers, Series B, 73-725, pp.380-386

[3] [10] Kastengren, A. L., Powell, C. F., Im, K.-S., Wang, Y.-J., Wang, J., 2009. "Measurement of Biodiesel Blend and Conventional Diesel Spray Structure Using X-Ray Radiography", Journal of Engineering for Gas Turbines and Power, Vol.131, pp.0628021-0628027.

- Edited Book:

[4] Yeh, C., N., Kosaka, H., Kamimoto, T., 1996. Measurement of Drop Sizes in Unsteady Dense Sprays, in "*Recent Advances in Spray Combustion: Spray Atomization and Drop Burning Phenomena*", Kuo, K., Editor. AIAA, Vol.1, pp.297-308.

[5] Hayami, H., Hirashima. K., 1987. Velocity Measurements in Combustion Fields Using a Laser-2-Focus Velocimeter, in "*Laser Diagnostics and Modeling of Combustion*", Inamura, K., Editor. Springer-Verlag, pp.21-28.

- Symposium Proceedings:

[6] Fezzaa, K., Lee, W-K., Cheong, S-K., Powell, C.F., Lai, M-C., Wang, J., 2005. "High-Pressure Diesel Injection Studied by Time-Resolved X-Ray Phase-Contrast Imaging", Proceedings of ILASS-Asia, pp.209-212.

[7] Choongsik, B., Jun, Y., Jangsik, K., Kyeong, O, L., 2002. "Effect of Nozzle Geometry on the Common-Rail Diesel Spray", SAE Paper , No.2002-01-1625

[8] Takeda, T., Okumura, N., Senda, J., 2006. "Study on Droplet Measurement of Unsteady Diesel Spray Using Phase Doppler Anemometry (PDA)" , Proceedings of ICLASS, ICLASS-06-118, p.233.

[9] Han, J-S., Lu, P-H., Xie, X-B., Lai, M-C. Henein, N.A., 2002. "Investigation of Diesel spray Primary Break-up and Development for Different Nozzle Geometries", SAE Paper No.2002-01-2775

[10] Lacoste, J., Crua, C., Heikal, M., Kennaird, D., Gold, M., 2003. "PDA Characterisation of Dense Diesel Sprays Using a Common-Rail Injection System", SAE Paper , No.2003-01-3085 , pp.2074-2085.

[11] Shodl, R., 1974. "L2FA Laser-Dual-Beam Method for Flow Measurements in Turbomachines", ASME Paper No.74-GT-157.

[12] Chaves, H., Kirmse, C., Obermeier, F., 2001, "Velocity Measurements of Dense Diesel Sprays in Pressurized Air", Proceedings of Spray 2001, TU Hamburg-Harburg, pp. II. 2-1-II. 2-8.

[13] Schugger, C., Meingast, U., Renz, U., 2000. "Time-Resolved Velocity Measurements in the Primary Breakup Zone of a High Pressure Diesel Injection Nozzle", Proceedings of ILASS-Europe, Darmstadt, pp.1-5.
[14] Ueki, H., Ishida, M., Sakaguchi, D., 1994. "Simultaneous Measurement of Particle Size and Velocity by Laser 2-Focus Particle Analyzer", Proceedings of ICLASS 1994, pp.483-490.

5th BSME International Conference on Thermal Engineering

1.03

Defect Assessment in Structural Materials Using Thermal Imaging

Golam Newaz

Mechanical Engineering Department, Wayne State University, Detroit, MI 48202 USA

Abstract

Application of heat pulse on material surfaces are used in thermal imaging to detect surface as well as subsurface defects in structural materials. The decay of the temperature on surface if mapped using infrared imaging can provide information about the presence of defects. The surface temperature variation can be described and analyzed with one-dimensional heat diffusion model. Thermal diffusivity and thermal conductivity (which are related) of the material can have a strong influence on temperature mapping for the material. In composite materials with anisotropic properties three-dimensional heat flow requires more complicated analysis and interpretation. For this case a three-dimensional mathematical model for time-dependent surface temperature was developed using Green's function. Both for metals and composites, temperature-time plots can provide valuable information about time delay as it relates to defect depth. However, the deeper the defect, slower is the temperature rise at the surface. Consequently, the second derivative of the of the temperature vs. time function can clearly show the time delay with different defect depth for a generic composite material. b represents defect depth in the following figure. In this talk, examples of thermal imaging from metallic and composite material systems are presented. Implication of this technology for engine and structural materials for aerospace components are emphasized.

5th BSME International Conference on Thermal Engineering

1.04

Recent advanced non-contact 3D flow visualization and measurements techniques

Deog Hee DOH

Korea Maritime University,Korea

Abstract

(Not provided)

Available online at www.sciencedirect.com

SciVerse ScienceDirect

Procedia Engineering 00 (2012) 000–000

Procedia Engineering

www.elsevier.com/locate/procedia

5th BSME International Conference on Thermal Engineering

Stability theory and experiments in wall-turbulence

P.K. Sen*, S. V. Veeravalli and Ganapati Joshi#

Indian Institute of Technology Delhi, New Delhi - 110016, India

Abstract

Drag reduction is one of the most important areas of research. The main concept behind drag reduction is turbulence control. This could possibly be achieved in near wall turbulent flow by suppressing wall-mode instabilities (i.e., by interfering with the seeding mechanism of turbulence production). Wall-mode instabilities can be studied by applying hydrodynamic stability theory to wall bounded turbulent flows. It has been shown in Sen & Veeravalli, 2000 (*Sadhana*, 25, 423-437) that an anisotropic eddy viscosity model is crucial in capturing the wall mode instabilities. The main results of this theory are discussed and we present detailed experimental investigations carried out with the objective of verifying the Sen & Veeravalli theory.

Keywords: *Stability theory; wall-turbulence; T-S waves; eddy viscosity; turbulence control.*

Nomenclature

H	Channel half width	u	Velocity fluctuation
U	Instantaneous velocity	$\tilde{u}$	Velocity component due to organised disturbance
$\overline{U}$	Mean velocity		
U_o	Centreline velocity	f	Frequency of organised wave
V	Sectional average velocity	α	Wave number, complex
$\mathrm{Re} \equiv \frac{U_o H}{\nu}$	Reynolds Number (using U_o)	α_r	Wave number, real
		α_i	Wave number, imaginary
$R \equiv \frac{VH}{\nu}$	Reynolds Number (using V)	$\beta = 2\pi f$	Circular frequency
		k	Turbulent kinetic energy
c	Wave speed, complex	ε	Eddy viscosity
c_r	Wave speed, real	ε_d	Turbulent dissipation rate
c_i	Wave speed, imaginary	θ	Phase angle
c_g	Group velocity	ψ	Stream function
P	Instantaneous pressure	ϕ	Eigenfunction
p	Pressure fluctuation	λ	Anisotropy function
$\tilde{p}$	Pressure component due to organised disturbance	κ	von Kármán constant
		ν	Kinematic viscosity

*Corresponding Author. Tel: +91-11-26591179; fax: +91-11-26581119
E-mail address: pksen@am.iitd.ernet.in

#Current Address: Defence Institute of Advanced Technology, Pune – 411025, India

1. Introduction

The use of hydrodynamic stability theory to understand near wall turbulence was initiated by Malkus [1]. He conjectured that if the turbulent mean velocity profile is used in the Orr-Sommerfeld equation then it should be marginally stable. The results of Reynolds & Tiederman [2] showed quite conclusively the failure of Malkus's conjecture. Reynolds & Hussain [3-4] theoretically showed, using a three-way decomposition, that an extra term corresponding to the Reynolds stress appears in the governing equation for the disturbance. They used an isotropic eddy viscosity model for the Reynolds stress and obtained an extended Orr-Sommerfeld equation, however, they did not find any region of instability. Their experiments (Hussain & Reynolds, [5]) and theoretical results indicated that hydrodynamic stability theory may not be relevant to wall-turbulence. Sen & Veeravalli [6-7] considered the problem afresh and concluded that the inability of previous researchers to find any unstable modes was because of the selection of an isotropic eddy viscosity model, which is really not justified near the wall. Sen & Veeravalli [6-7] used a more realistic anisotropic eddy viscosity model (based on Pope, [8]) and found wall-mode instabilities. The solutions found by Sen & Veeravalli [6-7] mimicked some features of wall bounded turbulent flows like location of the production peak.

2. Sen & Veeravalli [7] Theoretical Formulation

Experimental results are based on Sen & Veeravalli [6-7], hence a brief outline of the theory is directly reproduced from Sen & Veeravalli [7] to provide the background in which the experimental results may be interpreted.

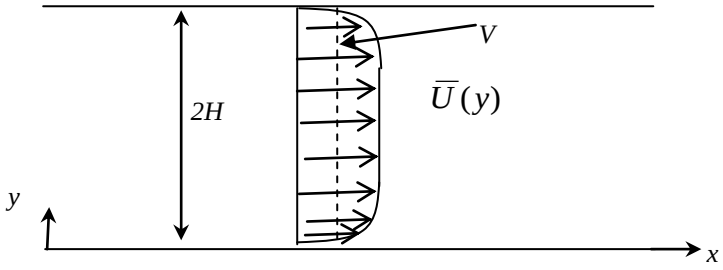

Fig.1. Turbulent channel flow

For the stability analysis the base flow is fully developed turbulent channel flow. In this an organised disturbance ($\tilde{u}$) is introduced. Thus Sen & Veeravalli (hereinafter denoted as S&V) [7] used a three way decomposition, similar to that of Reynolds & Hussain [3-4]

i.e. $$U_i = \overline{U}_i + \tilde{u}_i + u_i; \qquad P = \overline{P} + \tilde{p} + p \tag{1}$$

Where $\overline{U}_i, \overline{P}$ are respectively the time averaged velocity and pressure, $\tilde{u}_i$, $\tilde{p}$ are the contributions from the organised disturbance, and u_i, p are the respective turbulent fluctuations. Now by subtracting the time average of U_i from the ensemble (phase locked) average (denoted by $\langle\ \rangle$) the organised disturbance $\tilde{u}_i$ can be obtained. This procedure is true for pressure *P*.

i.e. $$\langle U_i \rangle - \overline{U}_i = \tilde{u}_i\,; \langle P \rangle - \overline{P} = \tilde{p} \tag{2}$$

By applying this procedure to the incompressible Navier-Stokes and continuity equations we get

$$\frac{\partial \tilde{u}_i}{\partial t} + \overline{U}_j \frac{\partial \tilde{u}_i}{\partial x_j} + \tilde{u}_j \frac{\partial \overline{U}_i}{\partial x_j} = -\frac{1}{\rho}\frac{\partial \tilde{p}}{\partial x_i} + \nu \frac{\partial^2 \tilde{u}_i}{\partial x_j \partial x_j} + \frac{\partial \tilde{r}_{ij}}{\partial x_j} \tag{3}$$

$$\frac{\partial \tilde{u}_i}{\partial x_i} = 0$$

Where $$\tilde{r}_{ij} = -\left(\langle u_i u_j \rangle - \overline{u_i u_j}\right) \tag{4}$$

The disturbance was assumed to be very weak compared to background turbulence i.e.

$$\left|\langle \tilde{u}_i \tilde{u}_j \rangle\right| << \left|\langle u_i u_j \rangle\right| \tag{5}$$

S&V [7] modelled the time-averaged Reynolds stress tensor using anisotropic eddy viscosity model outlined in Pope [8]. Pope's model for time averaged Reynolds stress tensor is:

$$-\overline{u_i u_j} = -\frac{2}{3}k\delta_{ij} + \varepsilon\bar{s}_{ij} - \varepsilon C(k/\varepsilon_d)\left[\frac{1}{2}\left[\bar{\omega}_{ij}\bar{s}_{kj} - \bar{s}_{ik}\bar{\omega}_{kj}\right]\right] \tag{6}$$

Here, the eddy viscosity ε defined as $-\dfrac{\overline{u\upsilon}}{(d\bar{U}/dy)}$; k is the turbulent kinetic energy; ε_d is the dissipation rate of the turbulent kinetic energy and C is a constant. From the form of the above equation S&V [7] defined an anisotropy parameter λ as $C(k/\varepsilon_d)(d\bar{U}/dy)$. Thus the standard isotropic form of the eddy viscosity model is recovered when λ is zero. The ensemble averages of the Reynolds stress similarly is modelled as:

$$-\langle u_i u_j\rangle = -\frac{2}{3}k\delta_{ij} + \varepsilon\langle s_{ij}\rangle - \varepsilon(\lambda/\bar{U}')\left[\frac{1}{2}\left[\langle\omega_{ik}\rangle\langle s_{kj}\rangle - \langle s_{ik}\rangle\langle\omega_{kj}\rangle\right]\right] \tag{7}$$

The model for $\tilde{r}_{ij}$ is obtained by subtracting Eq. (6) from Eq. (7).

Now, in order to obtain the general solution to Eq. (3), they considered normal modes of the form,

$$\psi = \phi(y)\exp^{i\alpha(x-ct)} \tag{8}$$

As shown in S&V [7], Squires theorem is weakly valid and hence only the 2D problem was considered. With these above formulation they obtained the following extended Orr-Sommerfeld equation. As is clear from Eq. (8) $\phi(y)$ is the eigenfunction, α is the wave number and c is the wave speed.

$$\begin{aligned}
&i\alpha^+\left[\left(\bar{U}^+ - c^+\right)\left(\phi'' - \alpha^{+2}\phi\right) - \bar{U}^{+\prime\prime}\phi\right] - \left[\phi'''' - 2\alpha^{+2}\phi'' + \alpha^{+4}\phi\right] \\
&-\left[E^+\left\{\phi'''' - 2\alpha^{+2}\phi'' + \alpha^{+4}\phi\right\} + 2E^{+\prime}\left\{\phi''' - \alpha^{+2}\phi'\right\} + E^{+\prime\prime}\left\{\phi'' + \alpha^{+2}\phi\right\}\right] \\
&-\lambda^+E^+\left[-2i\alpha^+\phi''' + 2i\alpha^{+3}\phi'\right] - 2i\alpha^+\phi'\left[\lambda^+E^{+\prime\prime} + 2\lambda^{+\prime}E^{+\prime} + \lambda^{+\prime\prime}E^+\right] = 0
\end{aligned} \tag{9}$$

The superscript '+' indicates that all the variables have been normalised by the inner scales. In Eq. (9), the first group of terms in square brackets corresponds to the Rayleigh equation; the first two groups of terms in square brackets correspond to the classical Orr-Sommerfeld equation; and, the remaining terms constitute the modifications to the classical Orr-Sommerfeld equation based on anisotropy.

Sen & Veeravalli [6-7] solved the above Eq. (9) for the turbulent boundary layer as well as for channel flow. They were able to show the presence of unstable modes (T-S like wall modes with the inner peak in the buffer layer) in the near wall region for a wave number band. Figure 2 shows nearly identical behaviour for turbulent boundary layer as well as channel flow.

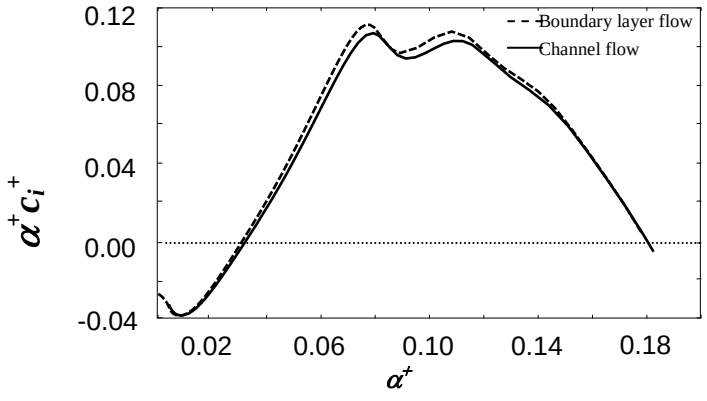

Fig.2. Growth rate curve from S&V [7], Reynolds Number is 5000 for both boundary layer and channel flow calculation.

3. Stability Experiments in a Turbulent Channel

Experiments were conducted to verify the results of S&V [7]. A 2-D channel was specially designed for this experiment.

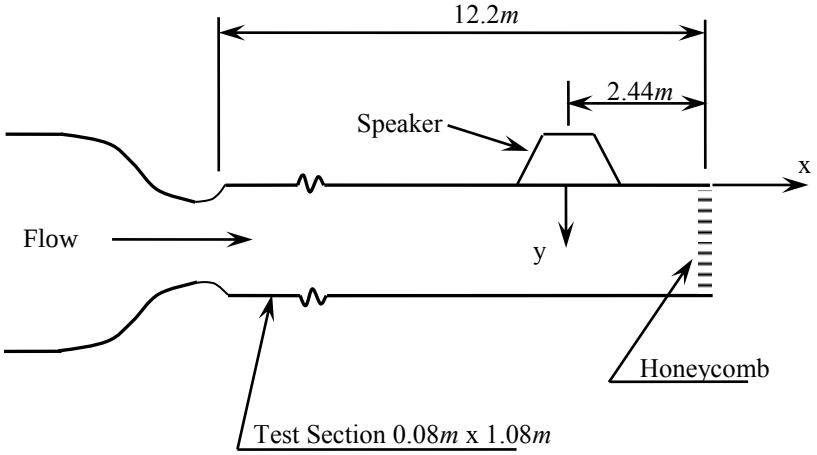

Fig.3. Schematic view of the set-up

Details about the experimental setup may be seen in Joshi [9]. Experiments were conducted for Re~14000. A hot-wire anemometer was used to obtain the turbulent data. The organised (sinusoidal) disturbance was generated by means of a speaker and was introduced through a span wise slot of size $1.5mm \times 100mm$ provided at the centre of the tunnel wall, $11.56m$ down stream of the entry to the channel. Different configurations were tried for introducing the organised disturbance. Three arrangements are shown in figure 4.

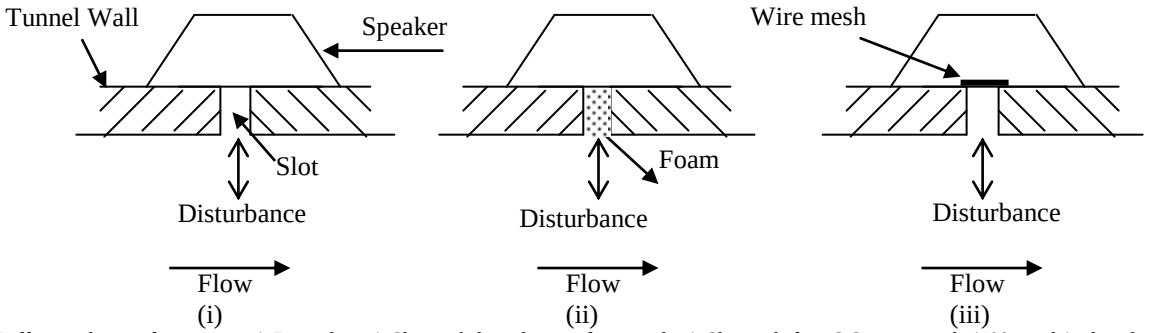

Fig.4. Different slot configurations. i) Bare slot; ii) Slot with low density foam and iii) Slot with fine S.S. wire mesh (400-grade) placed on the speaker side.

The configuration with the fine wire mesh (400-grade) was found to be the best setup for introducing the disturbance. A very detailed qualification was undertaken on the unperturbed and perturbed flow. Various checks were undertaken to ensure that the set-up and analysis procedures are adequate for resolving the organised disturbance and capturing its evolution. The detailed experimental results for all the above cases and qualification of the turbulent channel can be seen in Joshi [9].

The amplitude of the organised disturbance input to the speaker was set at 0.5V and the frequency was set to $300Hz$ for most of the experiments (the estimated wave number of this frequency is likely to lie close to the peak of the unstable range determined from S&V [7].

Repeatability of the eigenfunction was checked for organised disturbance of 300Hz, 0.5V and 7V. From figure 5a & 5b one can seen that degree of repeatability is remarkably good. In figure 5b results from an acoustic experiment (slot taped from out side, i.e. flow from the slot is blocked) shows the capability of the phase averaging method to extract even a very small disturbance due to vibration of the wall etc. As expected the amplitude of the eigenfunction for this case is very small (the peak value is approximately 20% of the amplitude of first two curves in figure 5b). The final curve in figure 5.b has been obtained with the speaker turned off. This result is an indicative of the error present in the phase-locked averaging process. As can be seen this error is quite negligible (less than 2.5% of the peak of the first curve). We are thus confident that our method of introducing the organised disturbance and extracting the eigenfunction through phase averaging is quite robust.

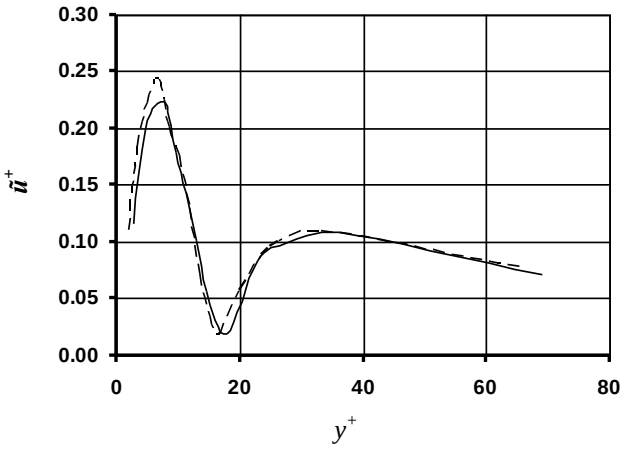

Fig.5a. Repeatability of the experiments. Dashed line and solid line shows the eigenfunctions measured on two different days with same hot-wire. Organised disturbance 300Hz 0.5V. Measurement station corresponds to $x = 10mm$.

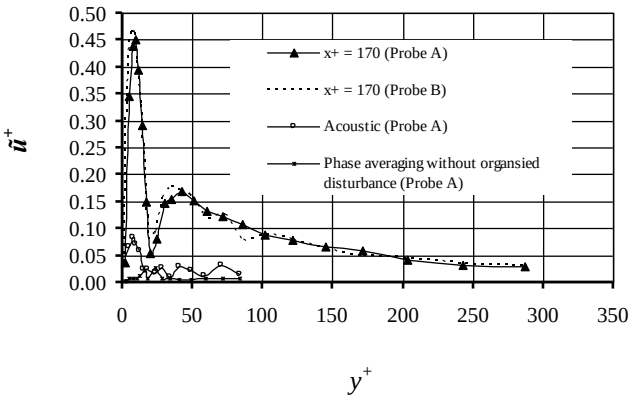

Fig.5b. Level of noise and acoustics on the eigenfunction. Organised disturbance 300Hz 7V Measurement station corresponds to $x = 10mm$.

4. Experimental Results & Discussion

Figure 6 shows a comparison between the calculated eigenfunction of S&V [7] with the experimentally obtained eigenfunction.

The non-dimensional wave number for the S&V [7] calculations has been set at $\alpha^+ = 0.057$, while, in the experiments it has been estimated to be approximately 0.058. Note that the vertical scale in the computations is arbitrary and it has been adjusted such that the magnitude of the inner peak of $\tilde{u}^+$ is the same as that in the experiments. We see that the eigenfunctions are qualitatively very similar. The location of the inner peak is slightly closer to the wall in the computations ($y^+ = 6.5$ as opposed to 8.0 in the experiments). Similarly the outer peak is also closer to the wall in the computations and its magnitude is lower. However, the location of the minimum in both cases is around $y^+ = 20$. The experimental eigenfunction extends much further into the body of the flow (beyond $y^+ = 300$). As discussed below this is probably due to several modes being excited by the speaker.

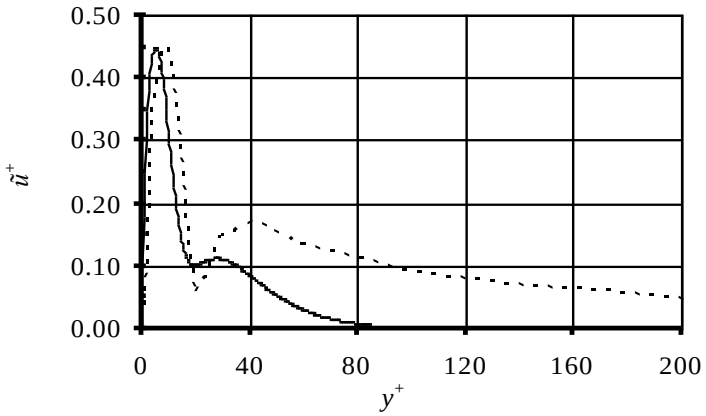

Fig.6. Comparison of our experimental eigenfunction (dotted line) with the theoretical results obtained by S&V [7], (solid line) at a Reynolds number of 5000, $\alpha^+ = 0.057$; $c_r^+ = 5.39$ and $c_i^+ = 1.05$.

Boundary excitation can generate different modes. Excitation can be from both sides, or can be from a single side. Hussain & Reynolds [5] used two sided excitation at low frequencies (25Hz to 100Hz) and obtained symmetric damped modes. In our present study, single sided excitation, at a higher frequency (as predicted by S&V [7]), resulted in unstable modes. Since the mode of interest is a wall mode, the outer boundary condition and the presence or absence of excitation in the other wall, should be irrelevant. It was not possible to modify our set-up to introduce two-sided excitation since the region of interest is

very close to the slot. However, in order to check the insensitivity of the measured eigenfunction to the outer boundary condition, we conducted experiments in a boundary layer of a wind tunnel (0.6m × 0.6m Test section). The organised disturbance was introduced through a speaker from the slot provided on the wall as in the case of the channel flow experiment. A comparison of the eigenfunctions obtained for the boundary-layer case and the channel case is shown in figure 7. The results show that the single side excitation is enough to get the TS-type wall mode. This is in agreement with the S&V [7] theory i.e., the eigenfunction for turbulent channel flow and boundary layer flow are similar.

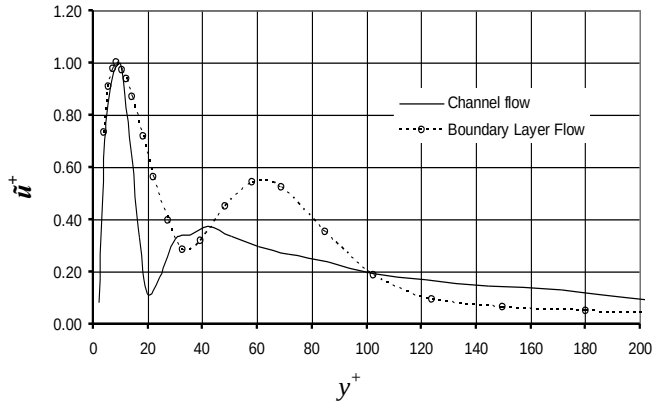

Fig.7. Eigenfunction for channel and boundary layer flow at a fixed disturbance frequency of 300Hz. Here the $\tilde{u}^+$ scaled arbitrarily to match the peak values. Measurement station corresponds to x = 10*mm*.

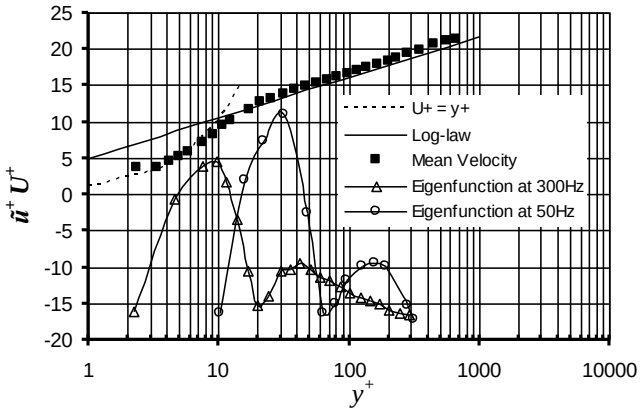

Fig.8. Mean velocity and Eigenfunction. Y- co-ordinate of the Eigenfunction is scaled such that it should appear with the mean velocity profile. Measurement station corresponds to x = 10*mm*.

Figure 8 shows a comparison between the modes obtained at 300Hz and 50Hz along with the mean velocity profile. It is clear that the wall mode (300Hz) has its primary peak in the buffer region, while the other mode (50Hz) which belongs to a class studied by Hussain & Reynolds [5], has its peak in the log region and where one will get only decay. Hence the modes studied by Hussain & Reynolds [5] are really not relevant to our work.

Another question is whether or not we can compare experimental (spatial) results with theoretical (temporal) results. So long as linear near-neutral disturbances are considered, spatial and temporal growth rates are related through the group velocity, c_g , as shown by Gaster [10]. In our problem we focus on mildly amplified near wall, boundary-layer like modes.

This being so, no appreciable difference is expected between spatial and temporal eigenfunctions. A comparison of $\tilde{u}_{rms}$ profiles obtained from theory for both temporal and spatial cases is shown in figures 9 below. To permit easy comparison, the $\tilde{u}_{rms}$ curves have been normalized by the maximum values of $\tilde{u}_{rms}$. The two curves are virtually identical.

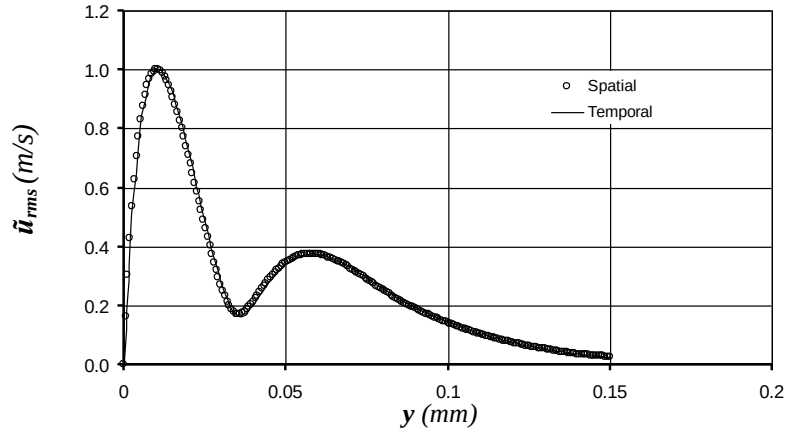

Fig.9. Graph of $\tilde{u}_{rms}$ versus y. For temporal case: α = 49, Re = 5000, c_r =0.35162439 and c_i =0.00601114. For spatial case: β = 17.2284, Re = 5000, α_r =49.3012 and α_i =-0.8135.

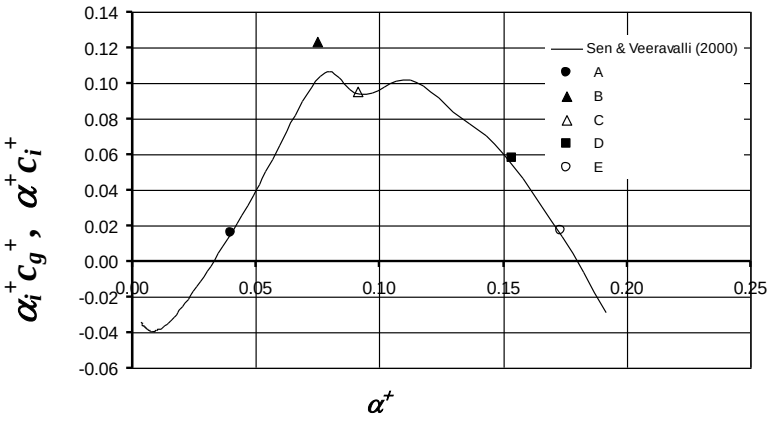

Fig.10. Growth rate curve $\alpha_r^+ c_i^+$ versus α_r^+ (inner variable scaling). Solid line is the temporal growth curve from S&V [7]. Symbols indicate the equivalent growth rate obtained for the 5 spatial cases studied (A to E). Reynolds Number is 5000.

Further we have chosen five different disturbance frequencies for comparing the growth rate obtained for the spatial and temporal calculations. The frequency values (labelled A, B, C, D and E) have been chosen such that they span the entire unstable range of the growth rate curve computed by S&V [7]. Except for one isolated case (near the most unstable region) the match is very good. Each from figure 9 and 10 it is clear that we can compare temporal growth rates from S&V [7] with our spatial growth rates from experiments over nearly the entire unstable band in α .

Evolution of eigenfunction was observed 3*mm* from the slot centre to about 12*mm* down stream. Figure 11a below shows measurements very close to the source of the disturbance (3*mm* to 8*mm*). At 3*mm* and 5*mm* it appears that there is competition between three modes, (i) the mode of interest which is a wall mode, (ii) another wall mode; and (iii) an outer mode. The second wall mode (ii) dominates at x = 3*mm*, decays rapidly, and effectively disappears by x = 8*mm*. The outer mode decays more slowly and is still visible in the profile at x = 8*mm*. The wall mode, of interest to us (i) is clearly discernible at x = 8*mm*. Note, x = 8*mm* corresponds to x^+ = 132 (1*mm* = 16.5 wall units). The normalised wave length, λ^+, of the organised disturbance (300Hz) is about 108. In our experiments, for all disturbance frequencies, we observed that the proper eigenfunction is obtained approximately 1.25 times the wavelength of the organised disturbance downstream of the slot. Klingmann et al. [11] observed a similar behaviour for TS waves in laminar boundary layer flow. Also the TS-like mode should show a π jump in the phase plot at the minimum of the eigenfunction.

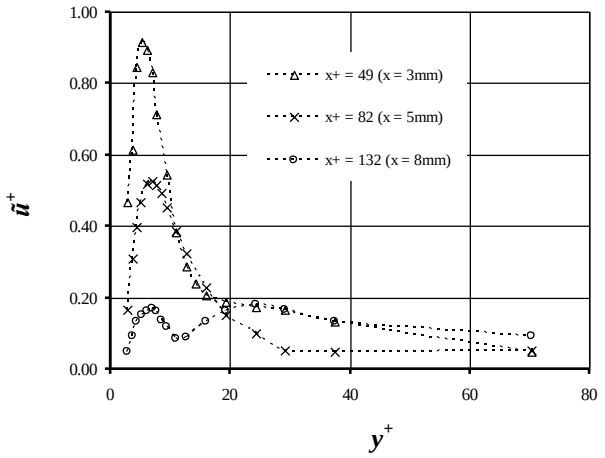

Fig.11a. Evolution of eigenfunction very close to the slot.

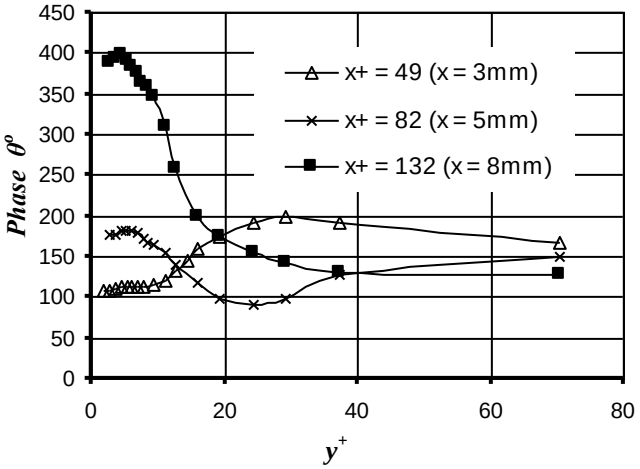

Fig.11b. Evolution of phase lag (θ)

One can see from figure 11b that there is no π jump at 3*mm* and 5*mm* but at 8*mm* there is a π jump. That means the required eigenfunction starts forming after 8*mm*. If we measure in the further downstream direction i.e. (8*mm* to 10*mm*) each of the curves in the figure 11c shows the presence of two peaks. In the first four stations the inner peak shows rapid growth, while, between the fourth and fifth stations the value of the inner peak remains unchanged. Each eigenfunction has a π jump at the minimum of the eigenfunction, as seen in figure 11d.

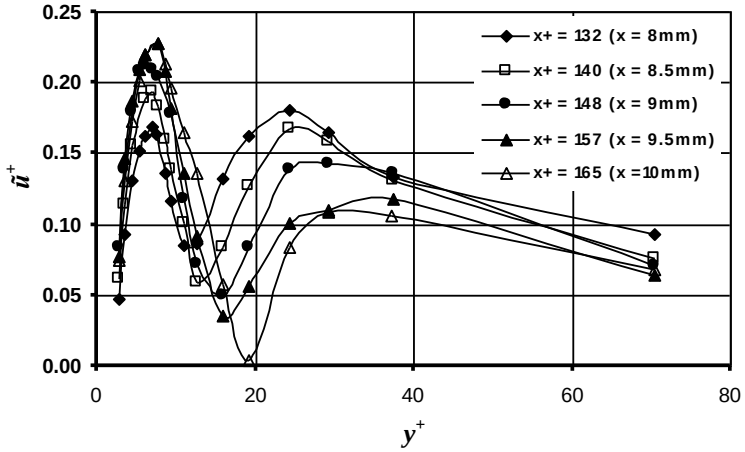

Fig.11c. Evolution of the eigenfunction in the vicinity of the slot.

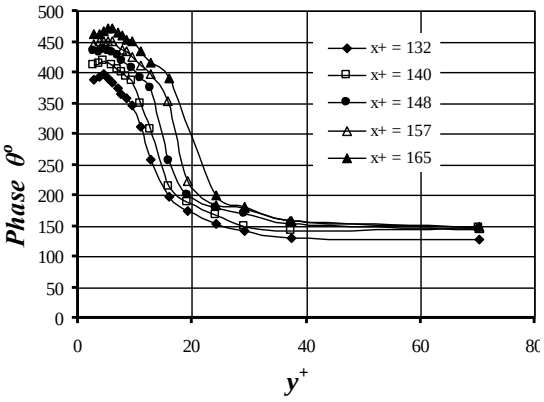

Fig.11d. Evolution of phase lag (θ)

Beyond $x = 10mm$ the inner peak also decreases and the location of the inner peak moves progressively away from the wall as shown in figure 11e.

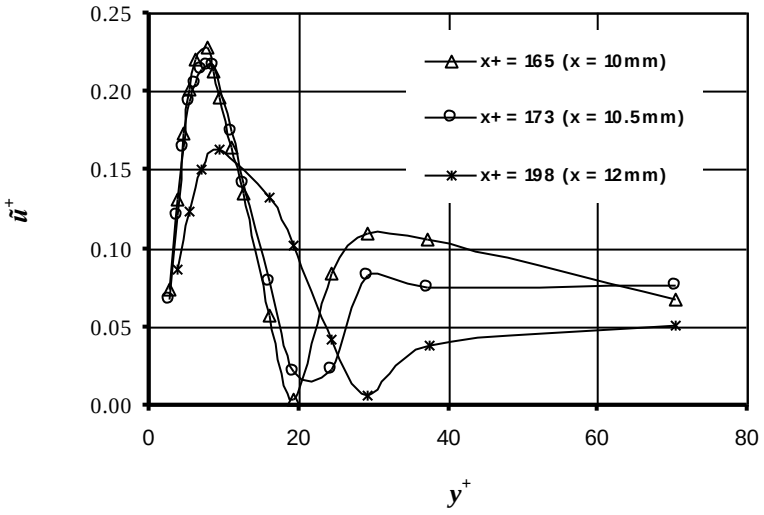

Fig.11e. Evolution of eigenfunction larger downstream distances.

In figure 12 the theoretical growth rate is shown as a function of the wave number. In this figure the points indicate the data obtained from the present experiments. Growth rates were calculated for different disturbance frequencies from 200*Hz* to 600*Hz* with amplitude of 0.5V. We see that the match between the experiments and the theoretical curve is quite good especially in the region where the curve is rising. Experiments at higher (>600Hz) frequencies indicate that the eigenfunction peaks shift towards the slot. Once the error bars are included, we see that the experimental growth rates are fully consistent with the theoretical curve obtained from S&V [7]. At lower frequencies (≤200Hz) the eigenfunction decay continuously and the growth rate is negative. On the other hand if we use the decay region (far down stream) of the data taken at 300*Hz* and calculate an effective growth rate (point 12 in figure 12) it does not lie anywhere near the theoretical curve. The linear theory presented in S&V [7] cannot explain a period of growth followed by decay.

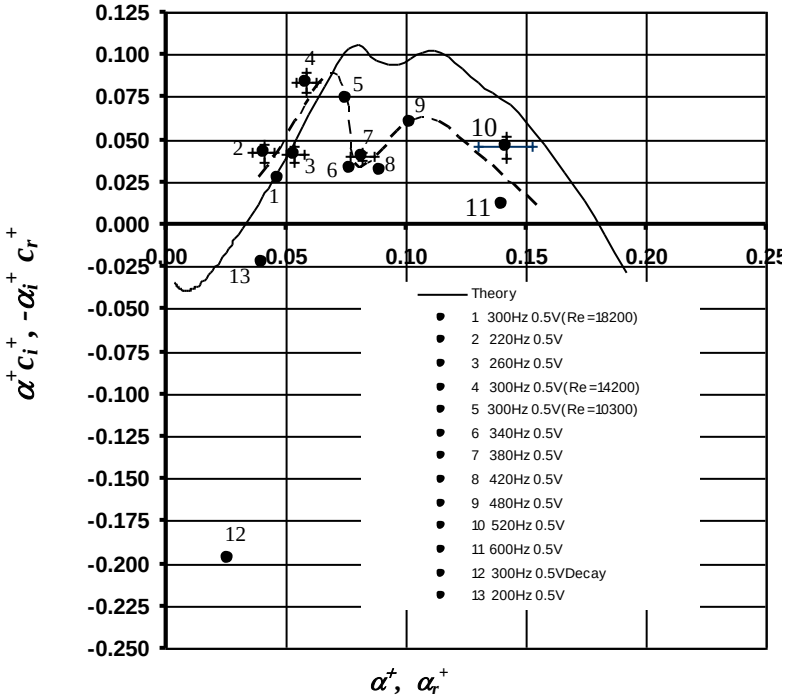

Fig.12. Growth rate curve $\alpha_r^+ c_i^+$ versus α_r^+ (inner variable scaling), Reynolds Number for the theoretical curve (solid line) is 5000. The curve is from S&V [7]. The points are from present experiments. The dotted line shows a rough trend passing through the experimental points. Unless explicitly mentioned the Reynolds number for the experiments is 14,000.

Figure 13 shows the evolution of the inner peak of the eigenfunction for different cases. The data at 300Hz show a clear region of growth followed by decay, while the data at 50Hz show uniform decay. One point of departure from S&V [7] is the decay observed in the experiments after an initial period of growth. Different ideas to explain the decay process were examined. Some candidates are; transient growth of non-normal modes, energy transfer between the organised disturbance and the corresponding disorganised disturbance (see chapter 5, Joshi [9]) etc. However the only possible explanation seems to be the break down of the two dimensionality of the instantaneous wave due to differential growth rates at different spanwise locations due to the presence of Klebanoff modes (K – modes). These are very similar to streaks in wall turbulence. A similar phenomenon was observed by Fasel [12] in his DNS work on a Klebanoff modes.

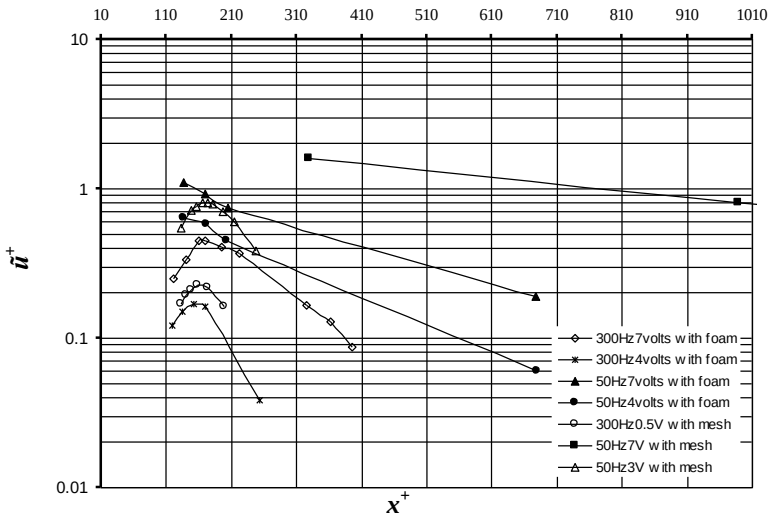

Fig.13. Evolution of inner peak of the eigenfunctions.

5. Conclusions

Our experimental results confirms the existence of TS – type modes in near wall turbulent flows and show fairly strong evidence in support of the theory outlined in S&V [6-7]. The eigenfunctions obtained in turbulent channel and boundary layer experiments are nearly identical, in the vicinity of the inner peak. This is consistent with the theoretical results of Sen and Veeravalli which show that the modes of interest are independent of outer boundary conditions. The shapes of the calculated and measured eigenfunctions are in good agreement. In the region of growth of the inner maximum the experimentally observed parameters (wave number, wave speed, growth rate and other parameters) are in good agreement with the theoretical results. Thus the claim made in S&V [6-7] that linear stability theory provides vital clues to understanding the mechanism of sustenance of turbulence in wall-bounded flows, has been corroborated.

Sen et al. [13] have shown that the interaction of 2D TS, 3D TS and Klebanoff modes can lead to explosive growth similar to the bursting phenomenon in wall turbulence. The 2D TS wave is a vital component of this mixture. Further Josan [14] and Sen et al. [15-16] have shown that the entire band of 2D TS waves could be suppressed by using compliant walls. This has serious implications for control of wall turbulence.

Acknowledgements

The support of the staff of the Gas Dynamics Laboratory (Dept. of Applied Mechanics, IIT Delhi), in particular Mr. R. P. Bhogal, is gratefully acknowledged.
An earlier version of this work was presented by Veeravalli et al. [17].

References

[1] Malkus W. V. R., 1956. Outline of a theory of turbulent shear flow, J. Fluid Mech., 1,521-539.
[2] Reynolds W. C., and Tiderman W. G., 1967. Stability of turbulent channel flow, with application to Malkus's theory, J. Fluid Mech., 27, 2, 253-272.
[3] Hussain A.K.M.F. and Reynolds W.C., 1970. The mechanics of an organized wave in turbulent shear flow, J. Fluid Mech., 41, 2, 241-258.
[4] Reynolds W.C. and Hussain A.K.M.F., 1972. The mechanics of an organized wave in turbulent shear flow Part 3. Theoretical models and comparison with experiments, J. Fluid Mech., 54, 2, 263-288.
[5] Hussain A.K.M.F. and Reynolds W.C., 1972. The mechanics of an organized wave in turbulent shear flow Part 2. Experimental results, J. Fluid Mech., 54, 2, 241-261.
[6] Sen P.K. and Veeravalli S.V., 1998. On the behaviour of organized disturbances in a turbulent boundary layer, Sadhana, 23, 167-193.
[7] Sen P.K. and Veeravalli S.V., 2000. Behaviour of organized disturbances in fully developed turbulent channel flow, Sadhana, 25, 423-437.
[8] Pope S. B., 1975. A more general effective-viscosity hypothesis, J. Fluid Mech., 72, 2, 331-340.
[9] Joshi, G.N., 2011. Experimental investigations on the relevance of hydrodynamic stability theory to wall-turbulence, PhD thesis, IIT Delhi.
[10] Gaster M., 1962, A note on the relation between temporally-increasing and spatially-increasing disturbances in hydrodynamic stability, J. Fluid Mech., 14, 02, 222-224.
[11] Klingmann B. G. B., Boiko A. V., Westin K. J. A., Kozlov V. V. and Alfredsson P. H., 1993, Experiments on the stability of Tollmien-Schlichting waves, J. Fluid Mech., 12, 4, 493-514.
[12] Fasel H. F., 2002, Numerical investigation of the interaction of the Klebanoff-mode with a Tollmien-Schlichting wave, *J. Fluid Mech.*, 450, 1-33.
[13] Sen P.K., Veeravalli S. V., Carpenter P. W., Joshi G. and Josan P. S., 2007, Organised structures in wall turbulence as deduced from stability theory-based method, *Sadhana*, Vol. 32, Part 1 & 2, 51-64.
[14] Josan P. S., 2004, Suppression of wall turbulence using a compliant surface based on stability and turbulence analysis, *Ph.D. Thesis*, I.I.T. Delhi, New Delhi.
[15] Sen P.K., Josan P.S.,Veeravalli S. V., and Carpenter P. W., 2006, Suppression of wall turbulence by stability turbulence analysis using a compliant surface., Proc Indian Natn Sci Acad, 72, 3, 159-166. (http://www.insa.ac.in)
[16] Sen P.K., Josan P.S. and Veeravalli S. V., 2006, Suppression of wall turbulence based on stability and turbulence analysis using a compliant surface. 6th *IUTAM symposium on Laminar-Turbulent Transition*, Editor: R Govindarajan, Springer, 231-236.
[17] Veeravalli S V, Sen P K & Joshi G, Stability theory and turbulent wall flow, Proc. *37th National & 4th International conference on FMFP*, FMFP10 – KN -11, 1-10, December 16-18, 2010, IIT Madras, Chennai, India.

Available online at www.sciencedirect.com

SciVerse ScienceDirect

Procedia Engineering 00 (2012) 000–000

Procedia Engineering

www.elsevier.com/locate/procedia

5th BSME International Conference on Thermal Engineering

An overview of biofuel as a renewable energy source: Development and Challenges

Masjuki Hj. Hassan *, Md. Abul Kalam

Department of Mechanical Engineering, University of Malaya, 50603 Kuala Lumpur, Malaysia

Abstract

Depletion of petroleum derived fuel and environmental concern has promoted to look over the biofuel as an alternative fuel sources. But a complete substitution of petroleum derived fuels by biofuel is impossible from the production capacity and engine compatibility point of view. Yet, marginal replacement of diesel by biofuel can prolong the depletion of petroleum resources and abate the radical climate change caused by automotive pollutants. Energy security and climate change are the two major driving forces for worldwide biofuel development which also have the potential to stimulate the agro-industry. Nonetheless, there are other problems associated with biofuel usage such as automotive engine compatibility in long term operation and also food security issues that stem from biofuel production from food-grade oil-seeds. Moreover, severe corrosion, carbon deposition and wearing of engine parts of the fuel supply system components are also caused by biodiesel. Discussing all this advantages and disadvantages of biodiesel, it is comprehended that, a dedicated biodiesel engine is the ultimate solution for commercializing biodiesel. Brazil successfully boosted their bioethanol marketing by introducing flexible-fuel vehicles (FFV), which have a dedicated engine for both ethanol and gasoline. A similar approach can bring a breakthrough in biofuel commercialization and production. So dedicated biofuel engine is a challenge for mass commercialization and utilization of biofuel. In this lecture worldwide biofuel scenario is assessed by biofuel policies and standards. Different biofuel processing techniques are also summarized. Some guidelines on dedicated biofuel engine are prescribed. Minor modifications on the engine may not cost much; but continuous research and development is still needed.

Keywords: Biofuel; diesel engine; emission;

1. Introduction

Fossil fuels are widely used as transportation and machinery energy source due to its high heating power, availability and quality combustion characteristics, but its reserve is depleting day by day. The diesel engine was invented by Dr. Rudolph Diesel and it was run by peanut oil at the Paris Exposition in the year 1900 [1]. So it has been established from then that, high temperature of diesel engine is able to run on variety of vegetable oils [2]. Today diesel-powered vehicles represents about one-third of the vehicles sold in Europe and the United States and it is being predicted that the sales of diesel run automotives will rise from 4% in 2004 to 11% by 2012. As an alternative for petro diesel in the transportation sector, biodiesel can easily become the crucial solution for environmental problems. First, it does not require any engine

* Corresponding author. Tel.: +6-03-79674448; fax: +6-03-79674448
E-mail address: masjuki@um.edu.my

modifications; second it reduces greenhouse gas (GHG) emission substantially and finally it also improves lubricity. These factors has make biodiesel usage more adaptable and attractive to current energy scenario, which are to ensure energy security, environmental sustainability and also to boost rural development by shifting of power from petro to agro-industry, simultaneously.

However, the use of raw vegetable oils as fuel may give rise to a variety engine problem, such as coking of injectors on piston and head of engine, carbon deposits on piston and head of engine and also excessive engine wear [3-5]. In order to overcome these problems, many researchers had recommended the use of transesterified vegetable oils that can greatly reduce the viscosity of the oil and this transesterified vegetable oil is termed as biodiesel. Biodiesel (Greek, bio, life + diesel from Rudolf Diesel) refers to a diesel-equivalent, a processed fuel derived from a biological source.

Biodiesel is the common name for a variety of ester-based oxygenated fuels [6] from renewable biological sources. It can be made from processed organic oils and fats. In technical terms, biodiesel is a diesel engine fuel comprised of monoalkyl esters of long-chain fatty acids that is derived from vegetable oils or animal fats [7-10]. It is designated as B100 and must meet the ASTM D 6751 requirements [11] and transesterification is an esterification process of long chained triglycerides of vegetable oils into fatty acid methyl esters (FAME) which is coined as biodiesel. To date, many vegetable oils have been used to produce biodiesel namely Peanut, Rapeseed, Safflower, Sunflower, Soya bean, Palm, Coconut, Corn, Cottonseed and Linseed. There were also biodiesel produced from non-edible oils such as Mahua, Neem, Karanja and Jatropha, which become hype in the light of recent food versus fuel conflict [11, 12]. But this debate lost its ground as most of the government policies permits only 5-20% biodiesel blend (B5- B20) with petro diesel. In the last decade, biodiesel has been proved to be technically sound when blended in low percentage either of by field trials or by laboratory experiments.

1.1. Biofuel feedstocks and Utilization

The two most commonly use biofuel types are biodiesel and bioethanol which were derived mainly from vegetable oils, seeds and lignocelluloses. Biodiesel can be use to substitute diesel and bioethanol can be use in terms of petrol. Common biodiesel feedstock comes from plant oils like rapeseed, soybean, sunflower, palm and some other non-edible oils like Mahua, Neem, Karanja, Jatropha, Animal fats like beef tallow and used cooking oil can also be used as biodiesel after refining, while new sources like algae is considered to be the third generation of biofuel (source: Wikipedia). Biodiesel contains no petroleum, but it can be blended at any proportion with No. 2 diesel fuel to be used in diesel engines with little or no modification. Fuel grade biodiesels are produced through the transesterification process conforming to strict specifications such as ASTM D6751 in order to ensure proper performance and quality. On the other hand, bioethanol is made mostly from the fermentation of sugarcane, corn, wheat, maize and potatoes. Brazil has been successfully reduced their dependency on petrol by introducing fuel-flex vehicle which are modified for the use of bioethanol and also bioethanol-petrol blends.

1.2. Biofuel Development

1.2.1. Asia

Currently, Asia's largest biofuels producers are Indonesia, Malaysia, Philippines, Thailand, People's Republic of China and India [13]. In other words, Southeast Asian countries along with two economic giants, i.e. India and China are the only participants in the biofuel industry. While, Southeast Asian countries mainly focus on export, India and China are putting forth their biofuel programs to keep up with their bullish economic growth and to reduce petroleum dependency.

Malaysia: Malaysia and Indonesia are respectively the largest and second largest producer of palm oil in the world [14], jointly, they produces about 85 % of world's palm oil. Palm biodiesel production in Southeast Asia (SE Asia) is drastically rising due to its high potential and yield factor. The tropical climate suitable for palm growth and also the relative cheap labour of this region have made palm biodiesel production more appealing [15]. Malaysia's biodiesel production is mainly palm oil based; however, some initiative has been taken to introduce Jatropha for mass production. Palm oil is derived from the flesh of the fruit of the oil palm tree *Elaeis Guineensis*. Palm tree was originated from West Africa (more specifically Guinea Coast). It has been initially introduced in Malaysia as an ornamental plant in 1870's and in Thailand just before World War II. The first commercial plantation in Malaysia and Thailand has only started in 1960's [16]. Malaysia produces 0.5 million tons of waste cooking oil every year and a simple purification and conversion process of used palm and coconut cooking oil can easily recycled the waste into good quality biodiesel. But in January 2009, palm diesel production has

accelerated in Malaysia with Indonesia as raw palm oil price gone down 75% with respect to January 2008 [17].

Indonesia: According to Indonesia's Ministry of Energy and Mineral Resources, 520,000 tons of biodiesel were produced in 2007 which was equivalent to 590,000 kL. Indonesia has projected to achieve 2.41 million kL by 2010 and the country has already achieved 24.4% of its objective so far. To date, there are currently eight biodiesel plants and by 2011, there will be another 15 - 17 more, adding some 2 million kL to the total biodiesel production [13].

Thailand: Thailand has progressed well after setting a target in January 2005 to replace 10% of diesel by biodiesel by the year 2012. There were about 800 gas stations selling B5 blends in 2007. The steady progresses of Thailand and Indonesia in this sector were mainly due to the availability of different types of feedstock. Thailand's main biodiesel feedstock is palm but it also uses coconut, Jatropha and used cooking oil. For bioethanol production, the feedstock was mainly from molasses, cassava and sugarcane. On the other hand, Indonesian produces bioethanol from sugarcane and cassava. Conversely, the biofuel production in Malaysia was generally focused on palm biodiesel, this has make Malaysia more susceptible to the fluctuation of petroleum and palm oil (food grade) prices. This is mainly due to the versatility of palm oil usage, ranging from food product to biodiesel; thus, making it the most sought after vegetable oil in the world.

India: According to the International Energy Agency's report "World Energy Outlook 2007", the worldwide energy demand would be 50 % higher in 2030 than that of today. China and India alone were accounted for 45 % of the increase in demand in this scenario. Meanwhile, India's major source of energy is coal which is used for electricity generation and currently, petroleum is imported to cope with the growing demand for transport fuel. For India, its ethanol market is more mature than its biodiesel market. In 2003, the Ministry of Petroleum and Natural Gas has launched the first phase of the Ethanol Blended Petrol (EBP) Program that mandated the blending of 5% ethanol in gasoline for nine states (out of a total of 29) and four union territories (out of a total of 6) [18]. As India does not have any surplus on edible vegetable oil, their biodiesel production was mainly focused on non-edible vegetable oil such as Jatropha, Mahua, Karanja and Neem.

The National Mission on Biodiesel was launched in April 2003 and has identified Jatropha as the most suitable oil seed plant with aim of reaching the targeted 20 % (B20) by year 2012. To achieve this, the Government has targeted 11.2 million hector areas to be planted with Jatropha by 2012 to produce sufficient oil seeds to support the biodiesel requirements. The first two phases of demonstration projects were implemented [19].

Peoples Republic of China (PRC): Currently, 80% of (the) PRC's fuel grade ethanol was made from corn, while the rest was from wheat. Cassava and sweet Sorghum are used on experimental basis only. (The) PRC only uses the inferior corn for ethanol production to avoid using its food stock. All fuel grade ethanol production and selling is controlled by state owned companies. There are currently six (6) possible biofuel feedstock, i.e. corn-derived ethanol; cassava-derived ethanol; sweet sorghum-derived ethanol; soybean-derived biodiesel; Jatropha fruit-derived biodiesel; and used cooking oil-derived biodiesel [19]. (The) PRC is one of the world's largest importers of edible vegetable oils. The majority of biodiesel plants are small scale and do not operate all the time probably due to the lack of feedstock. It may be the result of the Government not providing incentives for the production of biodiesels [16]. Chinese biodiesel production is minimal compared with its ethanol production. According to USDA, their biodiesel production amounted to approximately 300,000 metric tons. Almost all production was based on animal fat or waste vegetable oils.

Table 1. A short summary of worldwide official biofuel targets [12, 20, 21]

Country	Official Biofuel Targets
Brazil	40% rise in ethanol production, 2005-2010; Mandatory blend of 20–25 % anhydrous ethanol with petrol; minimum blending of 3 % biodiesel to diesel by July 2008 and 5 % (B5) by end of 2010
Canada	5% renewable content in petrol by 2010 and 2 % renewable content in diesel fuel by 2012
European Union	10% in 2020 (biofuels); target set by European Commission in January, 2008
UK	5% by 2020 (biofuels, by energy content)

2. Worldwide Biofuel Policies & Standards

In this section, a thorough view on biofuel policies, targets and its standardization (especially on biodiesels) of **Malaysia:** The "National Biofuel Policy" was introduced by the Ministry of Plantation Industries and Commodities of Malaysia on 21 March, 2006. It has five strategic thrusts:

i. Biofuel for transport,
ii. Biofuel for industry,
iii. Biofuel technologies,
iv. Biofuel for export and
v. Biofuel for a cleaner environment.

However, the Envo Diesel (5% Palm Methyl Ester and 95 % Diesel) project has been aborted by Malaysian government as it has failed to market it in 2008 as planned in "The National Biofuel Policy" [21].

Indonesia: The Government of Indonesia established its first national policy on biofuels in 2006 by setting a target of replacing 10 % of transport fuel by biofuel by 2010. The national oil company Pertamina has started selling the B5 biodiesel blends commercially but has suffered serious financial losses due to the high feedstock price of biofuel. In order to compensate the losses, the blend ration was lowered to 1% now. This phenomena have plunged the Indonesian government to the target to 2.5% diesel excision by biodiesel and 3% gasoline by ethanol in 2010 [4].

Table 2. Biofuels policies in selected Asian countries [2, 11, 22]

Country	Targets for 1st-generation biofuels and plans for 2nd-generation biofuels	Blending mandate	Economic measures
(the) PRC	Take non-grain path to biofuel development	Ethanol: trial period of 10% blending mandates in some regions	Ethanol: incentives, subsidies and tax exemption for production Diesel: tax exemption for biodiesel from animal fat or vegetable oil
India	No target identified Promotion of Jatropha	Ethanol: blending 5% in gasoline in designated states in 2008, to increase to 20% by 2017	Ethanol: excise duty concession Ethanol and diesel: set minimum support prices for purchase by marketing companies
Indonesia	Domestic biofuel utilization: 2% of energy mix by 2010, 3% by 2015, and 5% by 2025 Seriously considering Jatropha and cassava	Diesel: blending is not mandatory but there is a plan to increase biodiesel blend to 10% in 2010	Diesel: subsidies (at the same level as fossil fuels)
Japan	Plan to replace 500 ML/year of transportation petrol with liquid biofuels by 2010. Promotion of biomass-based transport fuels	No blending mandate upper limits for blending are 3% for ethanol and 5% for biodiesel	Ethanol: subsidies for production and tax exemptions
Malaysia	No target identified Promotion of Jatropha, nipa, etc.	Diesel: blending of 5% palm oil in diesel	Diesel: plans to subsidize prices for blended diesel
Philippines	No target identified Studies and pilot projects for Jatropha	Ethanol: 5% by 2008; 10% by 2010 Diesel: 1% coconut blend; 2% by 2009	Ethanol and diesel: tax exemptions and priority in financing
Thailand	Plan to replace 20% of vehicle fuel consumption with biofuels and natural gas by 2012 Utilization of cassava	Ethanol: 10–20% by 2008 (Gasohol 95) Diesel: 5% (B5) mix in 2007 and 10% (B10) by 2011	Ethanol: price incentives through tax exemptions

Peoples Republic of China: The government of China is making E10 blends mandatory in five provinces that accounted for 16% of the nation's passenger cars.

India: The Indian government through its bioethanol program has called for E5 blends throughout most of the country and is targeting to raise this requirement to E10 and subsequently to E20. A 5 % target of bioethanol incorporation into transportation fuel was set by the sugar ethanol program. However, there were no direct financial assistance or tax incentives provided for the production or marketing of ethanol or ethanol blended petrol. On contrarily, financial support was provided for research and development in ethanol production that was undertaken by the public and private organizations.

3. Characterization of Biodiesel:

Quality standards for producing, marketing and storing of biofuel are being developed and implemented around the world in order to maintain the end product quality and also to ensure consumers' confidence. The US and EU standards are the most referred standards followed by standards from other biofuel producing nations. Basically, the majority of the standards have

similar limits for most of the parameters (i.e. sulfated ash, free glycerol content, copper strip corrosion, acid number, etc.); however, different definition for the term biofuel occurred. For instance, both fatty acid methyl esters (FAME) and fatty acid ethyl esters (FAEE) were accepted as biodiesel in the Brazilian and US biodiesel standards, whereas according to the current European biodiesel standard only fatty acid methyl esters (FAME) is applicable. A comparison of biodiesel standards was shown in Table 3 and a short discussion on key fuel properties of biodiesel and their standards in the EU and US standards were outlined below:

Flash point: Flash point is a measure of flammability of fuels and thus an important safety criterion for transport and storage. The flash point of diesels is half of that of biodiesel fuels and therefore it represents an important safety asset for biodiesel. The flash point of pure biodiesels is considerably higher than the prescribed limits, but can decrease rapidly with increasing amount of residual alcohol [5, 23].

Viscosity: The kinematic viscosity of biodiesel is higher than that of fossil diesel, and in some cases, at low temperatures biodiesel can becomes very viscous or even solidified. High viscosity can affect the volume flow and injection spray characteristics in the engine. At low temperature it may even compromise the mechanical integrity of the injection pump drive systems [24].

Sulphated Ash: Ash content is defined as the amount of inorganic contaminants such as abrasive solids and catalyst residues and the concentration of soluble metal soaps contained in the fuel. These compounds are oxidized during the combustion process to form ashes that were responsible for engine deposits and filter plugging [23].

Cloud Point: The behaviour of automotive diesel fuel at low ambient temperatures is an important quality criterion, as partial or full solidification of the fuel may cause blockage of the fuel lines and filters, leading to fuel starvation, problems of starting, driving and engine damage due to inadequate lubrication. The melting point of biodiesel products depends on chain length and the degree of saturation, where long chain of saturated fatty acid esters displaying unfavourable cold temperature behaviour [24].

Copper strip corrosion: This parameter describes the tendency of a fuel to cause corrosion to copper, zinc and bronze parts of the engine and storage tank. A copper strip is heated to 50°C in a fuel bath for three hours, followed by comparison with a standard strips to determine the degree of corrosion. Corrosion resulting from biodiesel might be induced by some sulphur compounds or by acids; hence this parameter is correlated with acid number [12].

Cetane number: The cetane number of a fuel describes its propensity to combust under certain conditions of pressure and temperature. High cetane number is associated with rapid engine start and smooth combustion. On the other hand, low cetane number causes deterioration in combustion behaviour and higher exhaust gas emission of hydrocarbons and particulate. In general, biodiesel has a slightly higher cetane numbers than fossil diesel. Cetane number increases with increasing length of fatty acid chain and ester groups, and is inversely related to the number of double bonds [12].

Water content and sediment: The Brazilian and American standards combine both water and sediment content into a single parameter, whereas the European standard treats water as a separate parameter with sediment as Total Contamination. Water is introduced into biodiesel during the final washing step in the production process and has to be reduced by drying. However, even if very low water content was achieved after production, it does not guarantee that a biodiesel fuels will still meet the specifications during combustion because biodiesel is very hygroscopic and it can absorb water in a concentration of up to 1000 ppm during storage. Once the solubility limit is exceeded (at about 1500 ppm of water in fuels containing 0.2 % of methanol), water will start to separate from the fuel and begin to deposits at the bottom layer of the storage tank [23]. Free water promotes biological growth, forming sludge and slime that in turn may cause blockage of fuel filters and fuel lines. Moreover, high water contents are also associated with hydrolysis reaction that is responsible for converting biodiesel to free fatty acids which is also linked to fuel filter blockage. It also promotes the corrosion of chromium and zinc parts within the engine and injection systems [12].

Carbon residue: Carbon residue is defined as the amount of carbonaceous matter left after evaporation and pyrolysis of a fuel sample under specific conditions. Although this residue is not solely composed of carbon, the term "carbon residue" is found in all three standards because it has long been commonly used. The parameter serves as a measure for the tendency of a fuel sample to produce deposits on injector tips and inside the combustion chamber when used as automotive fuel [12].

Acid number: Acid number or neutralization number is a measure of free fatty acids contained in a fresh fuel sample and of free fatty acids and acids from degradation in aged samples. If mineral acids are used in the production process, their presence as acids in the finished fuels is also measured with the acid number. It is expressed as mg KOH required for neutralizing 1 gm of FAME. Higher acid content can cause severe corrosion in fuel supply system of an engine.

Free glycerine: The content of free glycerol in fatty acid methyl ester (biodiesel) is dependent on the production process, and high values may be resulted from insufficient separation during washing of the ester product. Glycerol may also separate during storage once its solvent methanol has evaporated. Free glycerol will separate from the biodiesel and falls to the bottom of the storage or vehicle fuel tank, attracting other polar components such as water, monoglycerides and soaps. These components can lodge in the vehicle fuel filter and cause damage to the vehicle fuel injection system [25]. High free glycerol levels can also cause injector coking.

Total Glycerol: Total glycerol is the sum of the concentrations of free glycerol and glycerol bound in the form of mono-, di- and triglycerides. Its concentration depends on the production process. Fuels that do not meet these specifications are prone to coking; thus, may cause the formation of deposits on the injector nozzles, pistons and valves [26].

Phosphorus: Phosphorus in FAME stems from phospholipids (animal and vegetable material) and inorganic salts (used frying oil) contained in the feedstock. Phosphorus has a strong negative impact on the long term activity of exhaust emission catalytic systems.

Distillation temperature: This parameter is an important tool, like ester content, for determining the presence of other substance and in some cases meeting the legal definition of biodiesel (i.e. monoalkyl esters).

Oxidation stability: Given to their chemical composition, biodiesel fuels are more susceptible to oxidative degradation than fossil diesel fuel. This is especially true for fuels with high content of di -and higher unsaturated esters because the methylene groups adjacent to the double bonds are particularly susceptible to radical attack as in

4. Biodiesel Processing Technology

Biomass processing technologies have a long history of development. All biomass conversion technologies can be subdivided in two major categories - thermo-chemical conversion and biochemical conversion. Pyrolysis, gasification and liquefaction are the common thermo-chemical process to produce syn-oil, bio-syngas and bio-chemicals respectively, from biomass. On the other hand, biochemical conversion process produces bioethanol and biodiesel. Bioethanol is produced by either fermentation or hydrolysis from different sources such as sugarcane, maize, potatoes, wheat, etc. Biodiesel is produced by the transesterification process, which is actually an alcoholysis process that converts triglycerides of vegetable oil to fatty acid methyl/ ethyl esters by displacing alcohol from an ester by another alcohol [28]. Bioethanol is fungible to petrol which is used in spark ignition engine. Similarly, biodiesel is interchangeably for diesel which is widely used in compression ignition engines.

Transesterification of triglycerides are first conducted by E. Duffy and J. Patrick in 1853. Famous German inventor Rudolph Diesel invented the diesel engine in 1893 when his paper entitled 'The theory and construction of a rational heat engine' was published in the same year [13]. Modifications and continuous improvements had been carried out by several researchers on the transesterification process to obtained higher yield rate of biodiesel and generally, for commercial transesterification process, the catalytic method is widely used.

Table 3. Physicochemical properties of biodiesel and biodiesel standards around the world [4, 11]

Properties (units)	Malaysia	Indonesia	Thailand	USA	EU	Brazil
		Indonesian National Standardization Agency	E 14214	ASTM D6751	E 14214	ANP 42
Flash point (°C)	182 min.	100 min.	120 min.	130 min.	120 min.	100 min.
Viscosity at 40°C (cSt)	4.415	2.3- 6.0	3.5- 5	1.9- 6	3.5- 5	-
Sulphated Ash (% mass)	0.01 max.	max. 0.02	max. 0.02	0.02 max.	0.02 max.	0.02 max.
Sulphur (% mass)	0.001 min.	0.001 min.	0.001 min.	0.001 min.	0.001 min.	-
Cloud point (°C)	15.2	Max. 18	-	-	-	-
Copper corrosion (3hr, 50°C)	Class 1	Class 3	1	Class 3	Class 1	Class 1
Cetane number	-	51 min.	51 min.	47 min.	51 min.	-
Water content and sediment (vol.%)	0.05 max.	0.05 max.	-	0.05 max.	-	0.05 max.
CCR 100% (% mass)	-	-	Max. 0.3	0.05 max.	-	0.1 max.
Neutralization value (mg, KOH/gm)	-	-	-	0.05	0.05	0.08
Free glycerin (% mass)	max. 0.01	max. 0.02	max. 0.02	max. 0.02	max. 0.02	max. 0.02
Total glycerin (% mass)	max.0.01	max. 0.24	max. 0.25	max. 0.24	max. 0.25	0.38
Phosphorus (% mass)	-	max.10 ppm(mg/kg)	max. 0.001	max. 0.001	max. 0.001	-
Distillation temperature	-	<360°C	-	< 360°C	-	<360°C
Oxidation stability, hrs	-	-	6	3	6	6

For catalytic transesterification method, the catalyst used can be either homogeneous or heterogeneous. Homogeneous catalyst are mainly alkaline (e.g. sodium hydroxide, sodium methoxide and potassium hydroxide) [29] or, acidic (e.g. sulfuric acid, hydrochloric acid and sulfonic acid) [30] in nature. Enzymes, titanium silicates, alkaline earth metal compounds, anion exchange resins and guanidine heterogenized on organic polymers are some of the heterogeneous type of catalysts used for transesterification [31]. Different types of transesterification approaches are shown in Fig. 1.

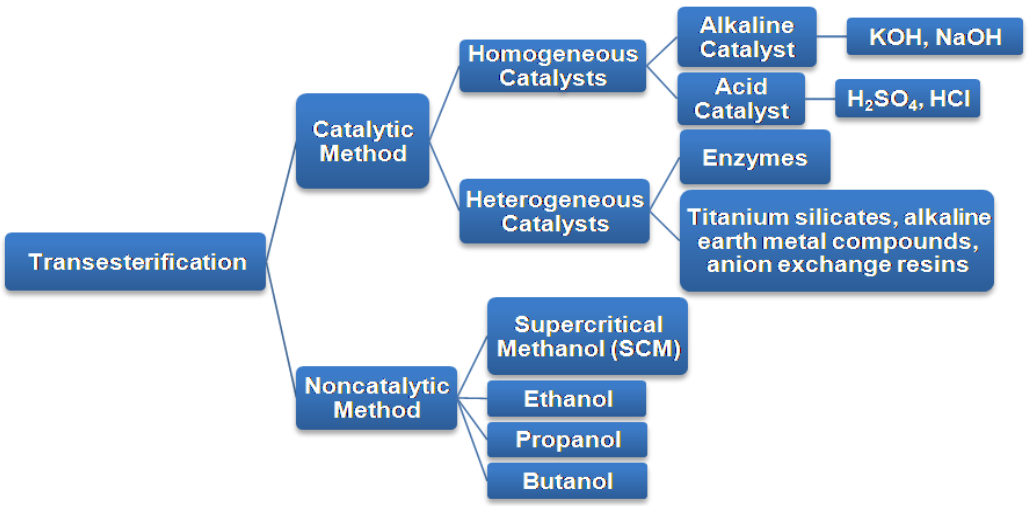

Fig. 1. Classification of Transesterification Processes

4.1. Catalytic method

For catalytic transesterification method, the catalyst is first dissolved into the methanol by vigorous stirring in a small reactor. Then, the oil that is to be transesterified will be transferred into a biodiesel reactor, followed by the catalyst/alcohol mixture. The final mixture is stirred vigorously for 2 hour at 340 K in ambient pressure. A successful transesterification reaction will produce two liquid phase: ester and crude glycerine. The crude glycerine, the heavier of the two liquid, will collect at the bottom after several hours of settling. Phase separation can be observed within 10 min and can be completed within 2 hour of settling; however, sometimes complete settling can take as long as 20 h. After the settling process is completed, water is added at a rate of 5.5% by volume of the methyl ester of oil followed by stirring for 5 min, before the glycerine is allowed to settle again. The washing step is a two-step process, which must be carried out with extreme care. A wash solution that comprised of 28 % water by volume of oil and 1 g of tannic acid per liter of water is added to the ester followed by gentle agitation. Air is carefully introduced into the aqueous layer while simultaneously stirring very gently. This process is repeated until the ester layer becomes clear. After settling step, the aqueous solution is drained, and only water is added at 28 % by volume of oil for the final washing step. An outline of the catalytic transesterification process is shown in Fig. 2.

Transesterification or alcoholysis is the usual conversion process used to convert triglycerides of vegetable oil to fatty acid methyl esters (FAME) by displacing alcohol from an ester by another alcohol [28]. For each triglyceride three monohydric alcohols reacts to produce (m) ethyl ester and glycerine (Fig. 3). An excess of alcohol is used to move this reaction towards the production side and catalysts are used to increase the reaction rate and yield of esters. Among the different type of catalysts used (i.e. alkali, acid and enzyme based), alkali based catalysts are most widely used in industrial processes because it is more effective [32] and less corrosive to the industrial equipment [33].

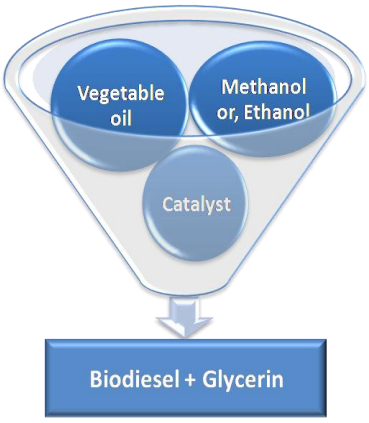

Fig. 2. Catalytic Transesterification

4.2. Non-catalytic method

The Transesterification of triglycerides by supercritical methanol (SCM), ethanol, propanol and butanol has proved to be the most promising process because of its higher yield of biodiesel obtained in a shorter period. The non-catalytic biodiesel production using supercritical methanol consists of a simple process and its higher yield production is due to the simultaneous Transesterification of triglycerides and methyl esterification of fatty acids [34]. The reaction mechanism of vegetable oil in SCM was proposed based on the mechanism developed by Krammer and Vogel [35] for the hydrolysis of esters in sub/supercritical water. The basic idea of supercritical treatment is based on the effect of the relationship between pressure and temperature upon the thermo physical properties of the solvent, such as dielectric constant, viscosity, specific weight and polarity [36]. Supercritical transesterification is carried out in a high-pressure reactor (autoclave).

The autoclave is heated by an external heater for about 15 minutes. The temperature of the reaction vessel can be measured by an iron-constantan thermocouple and maintained at approximate 5 K for 30 minutes. The transesterification reaction

occurs during this period. At the end of each run, gas is vented out and the transesterified product is transferred into a collecting vessel. All the contents are emptied out from the autoclave by washing with methanol.

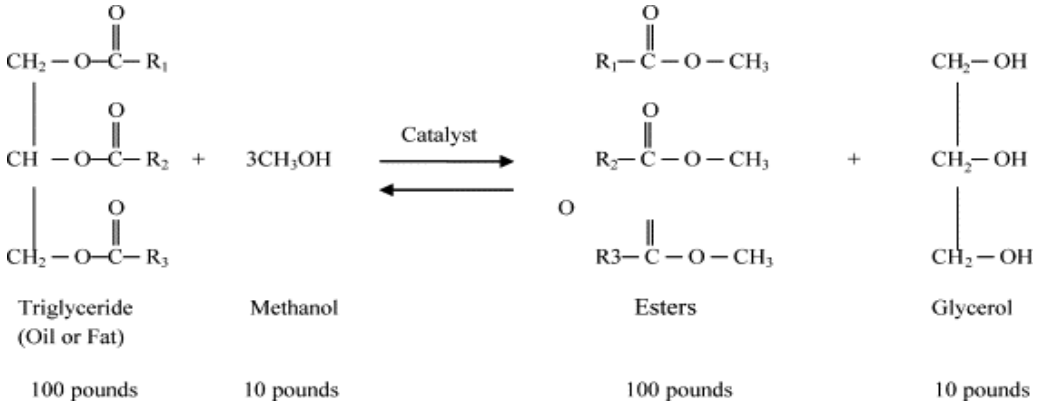

Fig. 3. Stoichiometric transesterification reactions

4.3 Factors affecting transesterification process

Several aspects such as the type of catalyst used, the molar ratio of alcohol to vegetable oil, temperature, water content and free fatty acid content have significant influence on the production rate and the quality of the produced biodiesel.

5. Advantages and Disadvantages of Biodiesel

Biodiesel have some advantages and disadvantages [2, 5, 11] which are listed as follows:

5.1. Advantages of Biodiesel:

1. Portability, availability and renewability of biodiesel.
2. Biodiesel emits fewer emissions such as CO_2, CO, SO_2, PM and HC compared to diesel.
3. Producing biodiesel is easier than diesel and is less time consuming
4. Biodiesel can make the vehicle perform better as it has a Cetane number of over 100. Moreover, it prolongs engine life and reduces the need for maintenance (biodiesel has better lubricating qualities than fossil diesel).
5. Owing to the clarity and the purity of biodiesel, it can be used without adding additional lubricant unlike diesel engine.
6. Biodiesel hold a great potential for stimulating sustainable rural development and a solution for energy security issue.
7. Biodiesel does not need to be drilled, transported, or refined like diesel.
8. Biodiesel is more cost efficient then diesel because it is produced locally.
9. Biodiesel is better than diesel fuel in terms of sulfur content, flash point, aromatic content and biodegradability.
10. It is safer to handle, being less toxic, more biodegradable, and having a higher flash point.
11. Non-flammable and non-toxic, reduces tailpipe emissions, visible smoke and noxious fumes and odors
12. No required engine modification up to B20.
13. Higher combustion efficiency

5.2. Disadvantages of Biodiesel:

1. It emits Higher NOx emission than diesel.
2. Higher pour and cloud point fuel freezing in cold weather causing a cold weather starting.
3. Biodiesel has a corrosive nature against copper and brass.

4. The high viscosity (about 11–17 times greater than diesel fuel) due to the large molecular mass and chemical structure of vegetable oils leads to problems in pumping, combustion and atomization in the injector systems of a diesel engine.
5. Biodiesel lower engine speed and power. The biodiesels on the average decrease power by 5% compared to that of diesel at rated load
6. degradation of biodiesel under storage for prolonged periods
7. Coking of injectors on piston and head of engine.
8. The high viscosity, in long term operation introduces the development of gumming, formation of injector deposits, plugging of filters, lines and injectors, ring sticking as well as incompatibility with conventional lubricating oils.
9. Carbon deposits on piston and head of engine.
10. Biodiesel causes excessive engine wear
11. Biodiesel is not cost-competitive with gasoline or diesel.

5. 3. Environment and Establishment

Palm oil is one of the most rapidly expanding crops in the world and it is posing a threat to the biodiversity of the Southeast Asian rain forests due to its huge environmental impact triggered by the growing market demand and higher yield factor [37, 38]. Problem started when, to increase palm oil production to keep up with the international demands become a national policy; hence, rainforest has been clear out to make way for palm plantation either by logging or burning. Moreover, wastage from palm mills creates huge water pollutions that negatively impacted the aquatic biodiversity. Other potential pollutants include palm oil mill effluents (POME), fertilizers, insecticides, rodenticides and herbicides [4]. The Malaysian government has recently announced that it will ban the conversion of 'protected forests' and 'forest reserves' to oil palm plantations and will only allow areas zoned for agriculture to be developed. Policy development and implementation should not only focus on higher production rate but must also take into account the conservation of forest and environment as well. Many researchers have claimed in GHG saving by biofuel, but very few have actually done a complete analysis of the total life cycle of biofuel from farm to 'burn'. Therefore, a comprehensive comparative factors analysis of life cycle of both petroleum based fuel and biofuel is vital to draw a bottom line about GHG saving or not. A more detailed life cycle based on GHG emission for both petroleum based fuel and biofuel is shown in Fig. 4.
Unfortunately, most of the papers stated some percentage of GHG savings without mentioning what are the factors they have considered other than a clear comparison of petro diesel vs. Biodiesel engine emission only. Generally, about 40-80 % reduction of engine emissions are reported by most papers using biofuel, but very few discussed what their assessments is

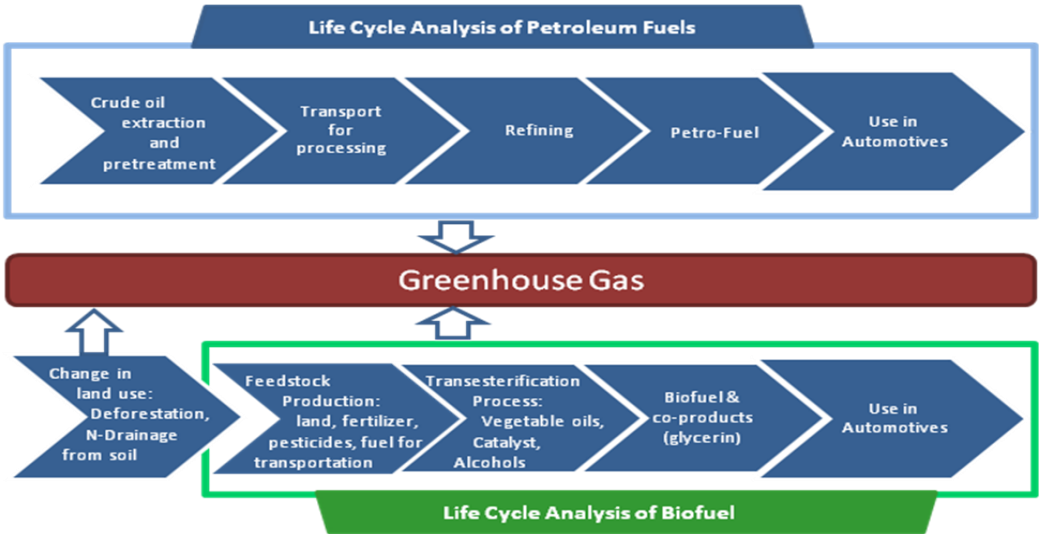

Fig. 4. Life cycle analysis of greenhouse gas balances of biofuel and petro-fuel

based on. There was an attempt to measure GHG emission for using palm oil in electricity production in comparison to coal based electricity production where a 50 % reduction has been reported.

5. 4. Major Engine Problems of using Biodiesel

In an effort to determine long term effect of biodiesel on engine, researcher have addressed following fuel properties of fatty acid methyl esters which required to be tailored properly for engine compatibility.

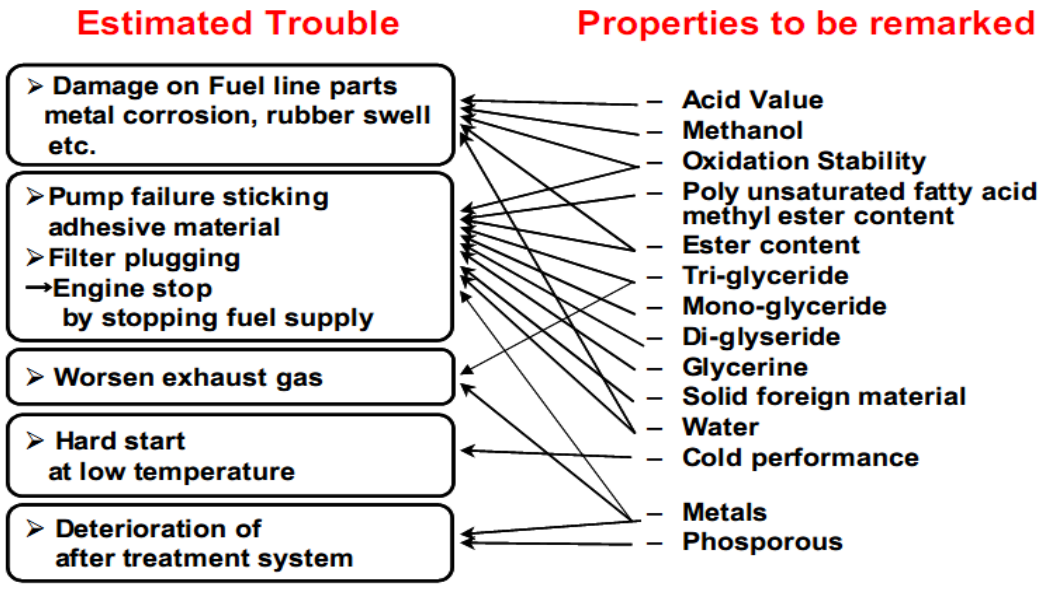

Fig. 5. FAME Properties to be remarked and the Estimated Impacts

6. A Comprehensive Solution-Biofuel Engine

Biofuel have many advantages as well as disadvantages; however, for marketing it, it requires certification from the engine manufacturers as adaptable fuel. But many engine fouling and complain caused by biofuel which are not possible to completely sort out without engine medication.

Brazil successfully utilized it vast agricultural resources and has uses bioethanol in highest proportion in their flexible-fuel vehicle (FFV) or dual-fuel vehicle. Bioethanol, being highly corrosive and hygroscopic can caused a lot of engine problems, thus to overcome this problem, the FFV uses a different fuel system that can adapt with bioethanol (E85). Moreover, the Flex-fuel engines are capable of burning any proportion of the resulting blend in the combustion chamber as its fuel injection and spark timing are automatically adjusted according to the actual blend detected by an electronic sensors.

Biodiesel may have to overcome many challenges to become a feasible substitute for conventional petro diesel and by far, it has been commercialized by the government and has enjoyed high subsidies. The main hurdle in penetrating the market is the high production cost of biodiesel relative to petroleum where major factor affecting biodiesels price is its feedstock price [39]. In order to reduce cost, the transesterification process needs to be economical and high yielding. On the agricultural aspect, low manpower cost, tropical environment and high yielding oilseed crops are important factors for vegetable oil based biodiesel. From this biodiesel industry, smallholder farmers will be benefitted by generating employment and increasing rural incomes, but the scope of those benefits is likely to remain limited with current technologies [40]. Technological advancement through continuous research and development is another challenge. A modified biodiesel engine is the only solution to compensate engine compatibly problems caused by the high viscosity and high cetane number of biodiesel. The fuel supply system also requires modification especially in the fuel filter and fuel pump. Adjustment of injection timing is also needed as biodiesel have a higher cetane number where the injection timing should be retarded a

little. Even though biodiesel has lower energy content where the engine may loses some power, but it can runs quieter and the fuel burns cooler, thus reducing NO_x emissions. Fuel Injection Equipment (FIE) Manufacturers (Delphi, Stanadyne, Denso, Bosch) showed their concern on following fuel properties of biodiesel**:**

- Free methanol: Corrosion of fuel injection equipment
- Dissolved and free water: It causes reversion of biodiesel to fatty acid and finally results to filter plugging
- Free glycerin: Free glycerin corrodes non-ferrous metals, soaks cellulose filters, Sediments on moving parts and Lacquering which causes filter clogging, injector Coking.
- Mono and di-glycerides
- Free fatty acids: Provides an electrolyte and hastens the corrosion of zinc, salts of organic acids, Organic compounds formed. Final result is corrosion of fuel injection equipment, Filter plugging, sediments on parts.
- Total solid impurity levels
- Alkaline metal compounds in solution
- Oxidation and thermal stability

Fuel Pump also suffers badly while operating in biodiesel blends. A list of fuel pump problems is given below:

- Corrosion of fuel injection equipment components
- Elastomeric seal failures
- Low pressure fuel system blockage
- Fuel injector spray hole blockage
- Increased dilution and polymerization of engine sump oil
- Pump seizures due to high fuel viscosity at low temperatures
- Increased injection pressure

Even though various research approaches on troubleshooting the problems of biodiesel is being carried out, a definite solution for all of this may not be possible without a dedicated biodiesel engine. For example, the Brazil's flex-fuel vehicle that has a modified diesel engine that can use different biodiesel blends (i.e. B5 to B20). It is quite achievable by modifying the fuel supply system (fuel pump, filter, injector, fuel tank, fuel lines and injection controller). Project on dedicated biodiesel engine as such may spur the biodiesel production and usage along with a hike in automobile sales like Brazil, who produced 17 million FFV automobiles by 2009.

Some suggestions on modifications of a diesel engine to a dedicated biodiesel automotive engine are listed below [41]:

1. **Fuel Pump:** Pump material (like aluminum alloy, iron based alloy) should be changed to a more corrosion resistant material. To reduce the seizure of the pump, a heating system can be run by radiator's heat.
2. **Fuel Filter:** As prescribed by many automobile manufacturer and researchers, engine requires more frequent change of fuel filter while running on biodiesel. But this will incurs extra cost to user and also require regular inspection as well. So a reinforced fuel filter container (to prevent the crash of highly viscous biodiesel) and a smaller meshed fuel filter can provide a good solution to this problem (Fig. 6).

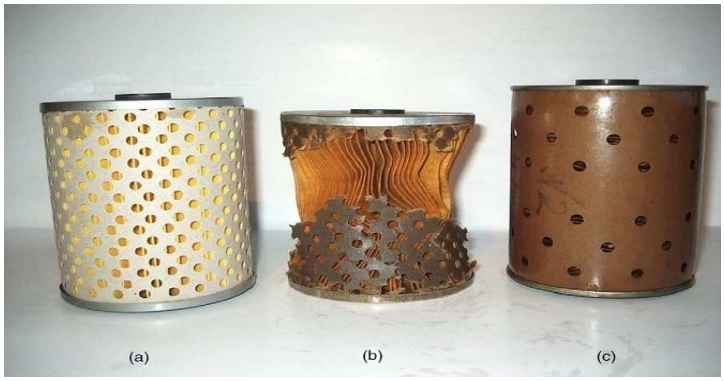

Fig. 6. The external view of a new fine porous filter element (a) that was damaged during experiments by pure rapeseed oil (b) in comparison with reinforced fielem (c) suitable to withstand oil pressure

3. **Fuel Injectors:** Jones et al. [42] have recommended that fuel injectors checking should be at least twice as often for biofuel user than that of diesel because of their coking and rapid ageing. Carbon deposition on the tip of injector is obvious, if the fuel used contains biodiesel even in minor proportions.
4. To avoid plugging and coke formation, the temperature of the nozzle has to be measured and kept (acting on the cooling water flow rate) below250 ◦C [43]. Such a nozzle design is proposed by Sgroi *et al.* [43], as shown in Fig.7.

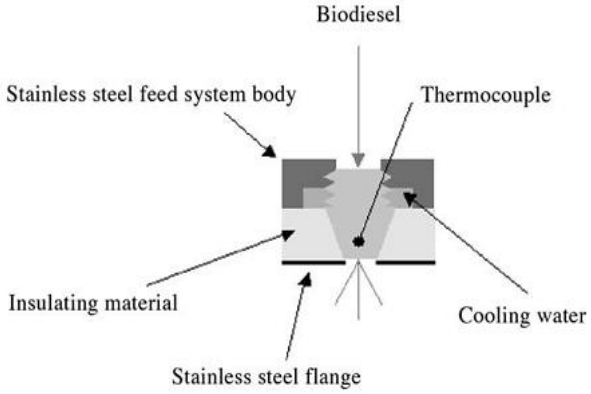

Fig. 7. Sgroi et al. proposed injector for biodiesel operation

7. Research on Biofuel in University of Malaya

University of Malaya has many academicians who are working on the research and development of the upcoming alternative fuel-biodiesel. For instance, the Department of Mechanical Engineering, the Department of Chemical Engineering and the Institute of Biological Science from the Faculty of Science are all currently working on different aspect of biofuel research.

7.1. Department of Mechanical Engineering

Department of mechanical engineering have a group of researchers devoted in continuous research and development of biofuels of various sources like palm, coconut, Jatropha, ethanol etc. Prof. Dr. Masjuki Hj. Hassan, Dr. Md. Abul Kalam and Prof. Dr. A.S.M.A. Haseeb have all been working on this alternative energy field for over ten years now. The research facilities and expertise of the Mechanical Engineering Department are in the engine tribology aspect (i.e. corrosion, wear and lubrication), various regulated (i.e. CO, HC, PM, NO_x, CO_2) and unregulated (i.e. PAH) engine emission, engine performance, endurance test, fuel deposition characterization and fuel and lube oil additives effectiveness measurement. A medium scale biodiesel plant was also installed to initiate the department's new research approach on biodiesel production processes.

7.2. Department of Chemical Engineering

Prof. Dr. Mohamed Kheireddine Aroua (Production/Process), Associate Prof. Ir. Dr. Abdul Aziz Abdul Raman (Production/Process), Prof. Dr. Nik Meriam Nik Sulaiman (Production/Process), Dr. Farouq Sabri Mjalli (Production/Process) and Prof. Dr. Mohd Ali Hashim (Process) has all contributed significantly to the research and development (R&D) of biofuel. The research facilities and expertise of the Department of Chemical Engineering pertaining to biodiesel lies in the processing technology, the separation process of transesterification, the use of different bio-catalyst, biodiesel production and also key fuel properties estimation-formulation-measurement for different feedstock and blends.
Associate Prof. Ir. Dr. Abdul Aziz Bin Abdul Raman

- Selective Purification of Biodiesel Using Inorganic Membrane, Principal Investigator (PI), 2009-2009.
- Production of Palm Biodiesel from RBD Palm Oil Using Continuous Membrane Reactor, Supervisor, 2008-2009, MOSTI.

- Production of palm biodiesel from RBD palm oil using continuous membrane reactor, Principal Investigator (PI), 2007-2009, MOSTI.

Prof. Dr. Nik Meriam Binti Nik Sulaiman

- Factors affecting the clouding of palm olein, Masters' Student Supervisor, 1998-1998, IPPP
- Conceptual study on life cycle assessment (LCA) of palm oil, PhD Supervisor, 2001-2001, PORIM Research Grant
- Life Cycle Studies (especially related to palm oil industries), PhD Supervisor, 2001-2005, Geran MPOB
- Experimental evaluation of tropical biomass burning emissions, Principal Investigator (PI), 2001-2005, IRPA.

7.3. Institute of Biological Science, Faculty of Science

Academicians from the Institute of Biological Science has been using a wide range of sources to produce biodiesel, ranging from waste vegetable oil to algae. Wastes from palm oil, corn oil, sunflower oil, soybean oil, canola, rice bran oil have been successfully converted into biodiesel after several treatments followed by the transesterification process. Beef tallow, chicken and fish by products are also used as feedstock for their new projects. The most recent project on biodiesel would be from algae where they have successfully produced a small amount of biodiesel from two local species.

8. Conclusions

Current trends in energy consumption are neither secure nor sustainable- environmentally, economically or socially. A forthcoming energy crisis will seize our social and economic growth if we do not change our usual practice and selection of energy source. Severe shortage of petroleum fuels is projected as inevitable in near future coupled with a drastic environmental implication. Hence, the hunt for an alternative clean fuel is vital. To date, wind, solar, tidal and fusion energy are all very prospective type of renewable energy. However, for a growing demand of transport fuel for millions of existing automobiles, we need an alternative that can easily adapt with the present supply and storing system and biofuel is such a candidate. Due to the fact that it is fungible to petrol and diesel in internal combustion engines with little modification.

Research has shown that internal combustion engines designed for petroleum fuels usage, which not suitable for long time operation on biofuel. Hence, a little modification can give a comprehensive solution in tailoring fuel properties for engine compatibility. And, Brazil has been the most successful nation in utilizing bioethanol with the introduction of its Flexi-fuel vehicles. On the contrary, to date, there is no modified vehicle patent that runs on biodiesel. Considering all the pros and cons and fuel properties this can be comprehended that multi-functional fuel additives may make biodiesels more engine compatible, but it will increases its price. So a mass production along with utilization needs a dedicated engine which could be done by modifying present day diesel engines on fuel supply system only.

Acknowledgment

The authors would like to acknowledge University of Malaya for financial support through High Impact Research Grant UM.C/HIR/MOHE/ENG/07.

References

[1]. Ghobadian, B., Rahimi, H., Nikbakht, A.M., Najafi, G.,Yusaf, T.F., 2009.Diesel engine performance and exhaust emission analysis using waste cooking biodiesel fuel with an artificial neural network, Renewable Energy 34, p. 976-982.

[2]. Silitonga, A.S., et al., 2011.A review on prospect of Jatropha curcas for biodiesel in Indonesia, Renewable and Sustainable Energy Reviews 15, p. 3733-3756.

[3]. Ma, F.,Hanna, M.A., 1999.Biodiesel production: a review, Bioresource Technology 70, p. 1-15.

[4]. Jayed, M.H., Masjuki, H.H., Saidur, R., Kalam, M.A.,Jahirul, M.I., 2009.Environmental aspects and challenges of oilseed produced biodiesel in Southeast Asia, Renewable and Sustainable Energy Reviews 13, p. 2452-2462.

[5]. Atabani, A.E., et al., 2012.A comprehensive review on biodiesel as an alternative energy resource and its characteristics, Renewable and Sustainable Energy Reviews 16, p. 2070-2093.

[6]. Atadashi, I.M., Aroua, M.K., Abdul Aziz, A.R.,Sulaiman, N.M.N., 2012.Production of biodiesel using high free fatty acid feedstocks, Renewable and Sustainable Energy Reviews 16, p. 3275-3285.

[7]. Shahabuddin, M., Kalam, M.A., Masjuki, H.H., Bhuiya, M.M.K.,Mofijur, M., 2012.An experimental investigation into biodiesel stability by means of oxidation and property determination, Energy.

[8]. Shahabuddin, M., et al., 2012.Effect of Additive on Performance of C.I. Engine Fuelled with Bio Diesel, Energy Procedia 14, p. 1624-1629.

[9]. Ghorbani, A., et al., 2011.A comparative study of combustion performance and emission of biodiesel blends and diesel in an experimental boiler, Applied Energy 88, p. 4725-4732.

[10]. Liaquat, A.M., et al., 2012.Application of blend fuels in a diesel engine, Energy Procedia 14, p. 1124-1133.

[11]. Mofijur, M., et al., 2012.Prospects of biodiesel from Jatropha in Malaysia, Renewable and Sustainable Energy Reviews 16, p. 5007-5020.

[12]. Jayed, M.H., et al., 2011.Prospects of dedicated biodiesel engine vehicles in Malaysia and Indonesia, Renewable and Sustainable Energy Reviews 15, p. 220-235.

[13]. Zhou, A.,Thomson, E., 2009.The development of biofuels in Asia, Applied Energy 86, Supplement 1, p. S11-S20.

[14]. Mofijur, M., et al., 2012.Palm Oil Methyl Ester and Its Emulsions Effect on Lubricant Performance and Engine Components Wear, Energy Procedia 14, p. 1748-1753.

[15]. Tan, K.T., Lee, K.T., Mohamed, A.R.,Bhatia, S., 2009.Palm oil: Addressing issues and towards sustainable development, Renewable and Sustainable Energy Reviews 13, p. 420-427.

[16]. Latner, K.C., O'Kray, C.,Jiang, J., 2006.(the) PRC bio-fuels. An alternative future for agricultural., USDA Gain report CH6049.

[17]. Hoekman, S.K., 2009.Biofuels in the U.S. – Challenges and Opportunities, Renewable Energy 34, p. 14-22.

[18]. Singh, S.K., 2007. India bio-fuels annual 2007, USDA Gain report IN7074.

[19]. Ou, X., Zhang, X., Chang, S.,Guo, Q., 2009.Energy consumption and GHG emissions of six biofuel pathways by LCA in (the) People's Republic of China, Applied Energy 86, Supplement 1, p. S197-S208.

[20]. López, J.M., Gómez, Á., Aparicio, F.,Javier Sánchez, F., 2009.Comparison of GHG emissions from diesel, biodiesel and natural gas refuse trucks of the City of Madrid, Applied Energy 86, p. 610-615.

[21]. Lopez, G.P.,Laan, T., 2008.Biofuels—at what cost? Government support for biodiesel in Malaysia. Prepared for the Global Subsidies Initiative (GSI) of the International Institute for Sustainable Development (IISD). Geneva, Switzerland.

[22]. Yan, J.,Lin, T., 2009.Biofuels in Asia, Applied Energy 86, Supplement 1, p. S1-S10.

[23]. Mittelbach, M., 1996.Diesel fuel derived from vegetable oils, VI: Specifications and quality control of biodiesel, Bioresource Technology 56, p. 7-11.

[24]. Rao, P.V., 2011.Experimental Investigations on the Influence of Properties of Jatropha Biodiesel on Performance, Combustion, and Emission Characteristics of a DI-CI Engine, World Academy of Science, Engineering and Technology 75, p. 855-868.

[25]. Mittelbach, M.,Gangl, S., 2001.Long storage stability of biodiesel made from rapeseed and used frying oil, Journal of the American Oil Chemists Society 78, p. 573-577.

[26]. Mittelbach, M., Wörgetter, M., Pernkopf, J.,Junek, H., 1983.Diesel fuel derived from vegetable oils: Preparation and use of rape oil methyl ester, Energy in Agriculture 2, p. 369-384.

[27]. Jain, S.,Sharma, M.P., 2010.Stability of biodiesel and its blends: A review, Renewable and Sustainable Energy Reviews 14, p. 667-678.

[28]. Srivastava, A.,Prasad, R., 2000.Triglycerides-based diesel fuels, Renewable and Sustainable Energy Reviews 4, p. 111-133.

[29]. Gryglewicz, S., 1999.Rapeseed oil methyl esters preparation using heterogeneous catalysts, Bioresource Technology 70, p. 249-253.

[30]. Furuta, S., Matsuhashi, H.,Arata, K., 2004.Biodiesel fuel production with solid superacid catalysis in fixed bed reactor under atmospheric pressure, Catalysis Communications 5, p. 721-723.

[31]. Vicente, G., Martínez, M.,Aracil, J., 2004.Integrated biodiesel production: a comparison of different homogeneous catalysts systems, Bioresource Technology 92, p. 297-305.

[32]. Formo, M., 1954.Ester reactions of fatty materials, Journal of the American Oil Chemists' Society 31, p. 548-559.

[33]. Murugesan, A., et al., 2009.Production and analysis of bio-diesel from non-edible oils—A review, Renewable and Sustainable Energy Reviews 13, p. 825-834.

[34]. Demirbaş, A., 2002.Diesel Fuel from Vegetable Oil via Transesterification and Soap Pyrolysis, Energy Sources 24, p. 835-841.

[35]. Krammer, P.,Vogel, H., 2000.Hydrolysis of esters in subcritical and supercritical water, The Journal of Supercritical Fluids 16, p. 189-206.

[36]. Kusdiana, D.,Saka, S., 2001.Kinetics of transesterification in rapeseed oil to biodiesel fuel as treated in supercritical methanol, Fuel 80, p. 693-698.

[37]. Fitzherbert, E.B., et al., 2008.How will oil palm expansion affect biodiversity?, Trends in Ecology & Evolution 23, p. 538-545.

[38]. Koh, L.P.,Wilcove, D.S., 2008.Is oil palm agriculture really destroying tropical biodiversity?, Conservation Letters 1, p. 60-64.

[39]. Graboski, M.S.,McCormick, R.L., 1998.Combustion of fat and vegetable oil derived fuels in diesel engines, Progress in Energy and Combustion Science 24, p. 125-164.

[40]. MacLean, H.L.,Lave, L.B., 2003.Evaluating automobile fuel/propulsion system technologies, Progress in Energy and Combustion Science 29, p. 1-69.

[41]. Masjuki, H.H., 2010.Biofuel Engine: A new challange, International & Corporate relation office, University of Malaya, Kuala Lumpur. ISBN (978-967-5148-65-1), p. 1-56.

[42]. Jones, S.T., Peterson, C.L.,Thompson, J.C., 2001. Used Vegetable Oil Fuel Blend Comparisons Using Injector Coking in a DI Diesel Engine An ASAE Annual International Meeting Presentation, Sacramento, California, USA. , p. 26.

[43]. Sgroi, M., Bollito, G., Saracco, G.,Specchia, S., 2005.BIOFEAT: Biodiesel fuel processor for a vehicle fuel cell auxiliary power unit: Study of the feed system, Journal of Power Sources 149, p. 8-14.